A NUCLEAR MAGNETIC RESONANCE PROBE OF Fe-Al AND $Al_{20}V_2Eu$ INTERMETALLICS

A Dissertation

by

JI CHI

Submitted to the Office of Graduate Studies of
Texas A&M University
in partial fulfillment of the requirements for the degree of

DOCTOR OF PHILOSOPHY

August 2007

Major Subject: Materials Science and Engineering

A NUCLEAR MAGNETIC RESONANCE PROBE OF Fe-Al AND $Al_{20}V_2Eu$ INTERMETALLICS

A Dissertation

by

JI CHI

Submitted to the Office of Graduate Studies of
Texas A&M University
in partial fulfillment of the requirements for the degree of

DOCTOR OF PHILOSOPHY

Approved by:

Chair of Committee,	Joseph H. Ross, Jr.
Committee Members,	Glenn Agnolet
	Donald G. Naugle
	Raymond E Schaak
Chair of Intercollegiate Faculty,	Joseph H. Ross, Jr.

August 2007

Major Subject: Materials Science and Engineering

ABSTRACT

A Nuclear Magnetic Resonance Probe
of Fe-Al and $Al_{20}V_2Eu$ Intermetallics. (August 2007)
Ji Chi, B.S., University of Science and Technology of China;
M.S., Texas A&M University
Chair of Advisory Committee: Dr. Joseph H. Ross, Jr.

Al-rich Fe-Al systems ($FeAl_2$, Fe_2Al_5 and Fe_4Al_{13}) and $Al_{20}V_2Eu$ have complicated structures with quasicrystal-like features making these materials potentially of interest for magnetic behavior. However, there is not much work on these materials. To study the variety of magnetic properties, we use NMR, magnetic susceptibility, specific heat and other methods in this work.

The microscopic electronic and magnetic properties of the Al-rich Fe-Al system and $Al_{20}V_2Eu$ have been studied via ^{27}Al NMR at temperatures between 4 and 500 K. The results of spin lattice relaxation rates reveal a pseudogap in Fe_4Al_{13} and Fe_2Al_5 around the Fermi-level in the density of states. Besides, a square well gap with a width of 2 meV and center at Fermi energy was detected by specific heat measurements in Fe_2Al_5. Both Fe_4Al_{13} and Fe_2Al_5 are non-magnetic systems with dilute magnetic defects, while $FeAl_2$ is a concentrated local magnetic moment system. In $Al_{20}V_2Eu$, a crossover was observed in NMR, magnetization and transport measurements. Above 40 K, Eu(2+) local magnetic moments dominate; below 40 K, a transition to a Kondo regime is observed, where the Kondo effect leads to the reduction of localized moments due to the formation of a spin-compensated Kondo cloud. With increasing magnetic field, f electrons participate more and more in excitations near the Fermi level and a heavy-Fermion state was observed through specific heat measurements at high magnetic field.

ACKNOWLEDGMENTS

I must first express my gratitude to my supervisor, Dr. Ross, whose expertise, understanding, and patience added considerably to my graduate experience. I would not have accomplished this without him. I'd like to thank many people I have worked with in Ross' group: Yang Li, Weiping Gou, Venkat Goruganti, Haidong Liu. I enjoyed the atmosphere, their friendship, and their support. It was a pleasure to work with all these people and to benefit from their knowledge. I wish to thank Daya Rathnayaka of Naugle's laboratory for helping to measure transport and heat capacity of this study.

I owe special gratitude to my family for continuous and unconditional support: To my parents for instilling in me confidence and a drive for pursuing my PhD and to my wife, Rong Li, for her enduring patience, understanding, and love.

TABLE OF CONTENTS

CHAPTER Page

I INTRODUCTION . . . 1

A. Materials Background . . . 3
1. Al-rich Al-Fe . . . 3
2. $Al_{20}V_2R$ . . . 7
3. Present Problem and This Study . . . 10

II NMR IN SOLIDS . . . 12

A. Spin Hamiltonian . . . 12
B. Knight Shift . . . 14
C. Line Shape . . . 17
D. Spin-lattice Relaxation Rates . . . 17

III BASIC THEORY OF NMR . . . 20

A. Motion of Free Spins . . . 20
B. FID and Spin-Echo . . . 21
C. Measurement of Spin-Lattice Relaxation . . . 23

IV EXPERIMENTAL APPARATUS . . . 24

A. NMR Spectrometer . . . 24
B. SQUID and PPMS . . . 25

V EXPERIMENTAL RESULTS AND DISCUSSIONS . . . 26

A. $FeAl_2$ . . . 27
1. Sample Preparation and Structure Analysis . . . 27
2. NMR Measurements . . . 27
B. Fe_4Al_{13} . . . 37
1. Sample Preparation and Structure Analysis . . . 37
2. NMR of Fe_4Al_{13} . . . 39
3. Specific Heat Measurements . . . 46
4. Magnetization Measurements . . . 50
C. Fe_2Al_5 . . . 55
1. Sample Preparation and Structure Analysis . . . 55
2. NMR of Fe_2Al_5 . . . 57

CHAPTER Page

3. Magnetization Measurements 57
4. Specific Heat Measurements 60
D. $Al_{20}V_2Eu_x$ 65
1. Sample Preparation and Structure Analysis 65
2. Magnetization Measurements 65
3. Specific heat Measurements 67
4. NMR Measurements 67

VI CONCLUSION 77

REFERENCES 79

VITA 89

LIST OF FIGURES

FIGURE		Page
1	Phase diagram of Fe-Al [18].	4
2	Fe_4Al_{13} structure. Small filled circles: Al(78/unit cell); large open circles: Fe (24/unit cell). Two cells shown, viewed along the b axis. Inscribed pentagons indicate the pentagonal and decagonal channels identified by Grin, *et al.* [12], the latter composed of stacked pentagonal anti-prisms.	5
3	Fe_2Al_5 structure: blue circles: Al(20 positions/unit cell); red circles: Fe(4/unit cell).	6
4	$FeAl_2$ structure. Filled circles: Fe (5/cell); open circles: Al (10/cell); dot-filled circles: mixed-occupancy sites (3/cell). (a) (021) plane, with frame showing a 3×3 set of triclinic unit cells. (b) View along (101) showing Fe pairs/triads. This Fe-containing layer alternates with an Al-only layer. (c) Rotated view of layer pictured in (b).	8
5	Cubic $Al_{20}V_2Eu$ structure: Eu nested in Al_{16} Frank-Kasper Friauf polyhedra, connected by a V-Al Kagom network	9
6	Powder x-ray results for $FeAl_2$, with results of refinement and difference plot. Vertical marks are fitted reflections.	28
7	^{27}Al NMR spectra for $FeAl_2$. Data offset vertically for clarity.	30
8	^{27}Al center-of-mass NMR shifts vs. temperature. Dashed curve: Curie-Weiss fit with $\theta = -38$ K.	31
9	$FeAl_2$ paramagnetic moment per Fe obtained from the magnetization curve, plotted vs. magnitude of effective on-site Al moment obtained from the mean NMR shift. Dashed curve is a least-squares linear fit.	32

FIGURE Page

10 ^{27}Al NMR FWHM linewidths for $FeAl_2$. Dashed curve is a Curie-Weiss fit with $\theta = -38$ K. 34

11 ^{27}Al NMR spin-lattice relaxation rate vs. T in $FeAl_2$. Dashed horizontal line shows T-independent local-moment behavior at high temperatures. Solid curve is a guide to the eye. 35

12 Powder x-ray results for Fe_4Al_{13}, with results of refinement and difference plot. 38

13 144 K ^{27}Al NMR powder pattern of Fe_4Al_{13} 40

14 Temperature dependence of relaxation rates for ^{27}Al. Solid curve: fits to the behavior described in the text. Inset: pseudogap around E_F corresponding to this fit. 42

15 ^{27}Al NMR shifts vs. temperature. Solid and dashed curves: fits described in the text, where dashed curve omits the Curie term. Inset: Temperature-dependence of ^{27}Al NMR linewidth, defined as full with at half-maximum of the NMR lineshape. 44

16 C/T vs. T^2 for Fe_4Al_{13} between 0 and 40 K in fields of 0 T and 8 T. The solid curve is the fitted function described in the text and the dotted curve is the difference between the fit and the zero-field data. 47

17 Temperature dependence of ΔC in fields of 0 T and 8 T below 20 K. Curves: fits to the Schottky function described in the text 48

18 Magnetic entropy extracted from specific heat in fields of 0 T (dashed curve) and 8 T (dotted curve) below 30 K. 49

19 The dc susceptibility $\chi(T)$, per mol Fe, in an applied field of 1000 G. Solid curve represents the Curie fit described in the text. Inset: χ^{-1} vs temperature, with curve corresponding to the the same fit. . 51

20 Magnetization per mol Fe vs. applied field. Data from top to bottom measured at $T = 30$, 40, 50, 180, 190, 200 K. Solid curves: paramagnetic behavior identified from low-T specific heat, with a single additive constant fitting parameter. Inset: Expanded view showing data for 180, 190, 200 K, with similar theoretical curves. . . 53

FIGURE Page

21 Saturation magnetization for ferromagnetic clusters in Fe_4Al_{13} obtained as described in text. Curve is mean-field saturation curve, intended to guide the eye. 54

22 Powder x-ray results for Fe_2Al_5, with results of refinement and difference plot. 56

23 Temperature dependence of relaxation rates for ^{27}Al. Solid curve: fits to the behavior described in the text. Inset: T_1 calculations. The dotted line is the calculation without the gap, the heavier solid line is the calculation with the gap, and open squares are experimental data. 58

24 The dc susceptibility $\chi(T)$ per mol of Fe in an applied field of 1000 G. The solid curve represents the Curie-Weiss fit described in the text. Inset: $\chi - \chi_d$ vs. temperature. 59

25 C/T vs. T^2 for Fe_2Al_5 between 0 and 30 K. The solid curve is the fitted function without gap described in the text. 61

26 $\Delta C/T$ vs. T for Fe_2Al_5 between 0 and 30 K. The solid circles are the experimental data, the open circles are the calculation results described in the text and the solid squares are the difference. 62

27 Pseudogap and the single sharp feature of DOS around E_F corresponding to the fits described in the text. Inset: the narrow and deep gap at Fermi level. 63

28 The dc susceptibility $\chi(T)$, per mol $Al_{20}V_2Eu_{0.7}$, in an applied field of 100 G. Dashed curve represents the Curie fit described in the text. Open squares represent the susceptibility results of $Al_{20}V_2La$. Inset: χ^{-1} vs temperature, with curve corresponding to the the same fit. 66

29 C/T vs. T^2 up to (32 K)^2 in fields between 0 T and 8 T. Dashed lines: $\gamma + \beta T^2$ fits for 0 and 8 T. Inset: Specific heat results at H = 0 T 68

30 γ vs. field. 69

FIGURE Page

31 295 K ^{27}Al NMR powder pattern of $Al_{20}V_2Eu_{0.7}$ 70

32 Temperature dependence of relaxation rates for ^{27}Al. Solid curve: fits to the behavior described in the text. 71

33 ^{27}Al NMR shifts and FWHM linewidths vs. χ for $Al_{20}V_2Eu_{0.7}$. 72

34 Experimental/theoretical magnetization ratios, described in text, for the indicated fields. Inset: DC susceptibility result at high magnetic fields. 74

35 Resistivity vs. temperature at different magnetic fields. 75

CHAPTER I

INTRODUCTION

Transition metal (TM) aluminides have a wide variety of atomic structures with unusual properties. They can form complex atomic structures ranging from solid solutions, disordered alloys and ordered compounds to quasicrystals. Besides being theoretically interesting due to their complicated atomic structure, their atypical electronic properties, reduced density of electronic states (DOS) at the Fermi level, as well as anomalous transport properties, have attracted more and more attention. These exceptional properties of Al-rich Al-TM systems — low electrical and thermal conductivity, unusual optical properties, low surface energy and coefficient of friction, oxidation resistance, biocompatiblity and high hardness — make them interesting for practical purposes. Also transition metal aluminides show a variety of magnetic behavior, from diamagnetic susceptibility with no localized moment, Curie-like behavior with some diluted localized moments, to ferromagnetism and spin-glass behavior at low temperature [1, 2, 3].

There have been many theoretical studies of the electronic structure of Al-rich Al-TM systems. General features of DOS in these Al(rich)-TM alloys include the following [4, 5]: At low energy, the states are mainly *sp* states. The *d* DOS peak of TM is in the middle of the *sp* band. The Fermi level(E_F) is found near a well-defined valley that splits the band between bonding and anti-bonding states. This valley, called a "pseudogap", that increases the stability of these structures, is generally attributed to a combined effect of the Hume-Rothery mechanism and the strong $sp - d$ hybridization. Sometimes instead of a pseudogap, a semiconducting gap is formed. The

---

The journal model is *IEEE Transactions on Automatic Control*.

width of the pseudogap varies from 0.3 to 1 eV. Experimentally the pseudogap has been observed in many different Al(rich)-TM samples either directly by photoemission, soft x-ray emission, and tunneling and point contact spectroscopy or indirectly via transport phenomena such as electrical conductivity and low-temperature specific heat that are compatible with an anomalously low DOS at E_F. The d DOS peak of the TM is located near E_F. The width of the d band varies with the TM element, mainly due to $sp-d$ hybridization. Moreover there is a significant contribution of the partial d DOS to the total DOS at E_F. Also, spectroscopy measurements [6, 7, 8] confirm the position of the d peaks, a strong $sp-d$ hybridization, a weak electron transfer between Al atoms and TM atoms, and the existence of a pseudogap near E_F.

However, in quasicrystals and approximants, there exists also an interesting theoretical predication that in additional to the global pseudogap at E_F, the calculated DOS displays around the Fermi level an unusual set of peaks and pseudogaps on the energy scale of 10 meV. Such sharp features is associated with bands of small-energy dispersion, yielding a low group velocity for the electron wave packets that could have a profound effect on the transport properties. The existence of fine spiky DOS could stem from the specific electronic localization at the presence of clusters of transition metals. Several experiments have tried to unveil this DOS feature, however, even high resolution photo-emission spectroscopy failed to detect the spiky DOS [9, 10]. It is possible that photo-emission spectroscopy analyzes the surface of the compounds, and the spiky structure could disappear at the surface because it should be very sensitive to the composition and the atomic structure. Or, the theoretical calculations do not take into account disorder and electron-electron interactions. Indeed, there is no current agreement on the source of this effect.

An effective TM-TM medium-range interaction is also related to the electronic structure of Al-TM alloys. This interaction is mediated by the Al atoms and its

medium-range character is due to the strong sp-d hybridization. Therefore, the positions of TM atoms in the structure is a determining parameter for the density of states, the magnetism and the stability. In the case of Mn aluminides, the most stable positions correspond to non-magnetic Mn, these positions correspond to positions that increase the pseudogap. A small proportion of Mn atoms are magnetic because they are located on less favorable positions [1].

A. Materials Background

1. Al-rich Al-Fe

The Al-Fe system is one of the transition metal aluminide systems and stable phases Fe_4Al_{13}, Fe_2Al_5 and $FeAl_2$ have been observed in this system, shown in the phase diagram, Fig. 1. Fe_4Al_{13} has a monoclinic structure ($mC102$, space group # 12) with 102 atoms per unit cell [11], shown in Fig. 2. There are 5 atomic sites for Fe, 15 sites for Al, while only one Al site shows partial occupation (92±2%). The main feature of the Fe_4Al_{13} structure is one-dimensional "channels", built of icosahedra and pentagonal prisms in different ratios [12]. So Fe_4Al_{13} can be considered as a decagonal approximant. Transport measurements showed anisotropic $\rho(T)$ behavior with metallic resistivity along the b axis and nonmetallic resistivity, $\rho(4.2K)/\rho(300K) \approx 2.5-5$, along the pseudo-quasi-periodic planes [13]. This special atom arrangement could lead to the formation of a pseudogap in this complex unit cell. Ab initio studies showed that complex monoclinic Fe_4Al_{13} is more stable than the simple tetragonal $FeAl_3$(Al_3V structure). Also a broad pseudogap around E_F is shown in electronic structure calculations, and DOS is around 14 states/eV unit cell at E_F [14, 15]. A sizable magnetic moment of 0.4 μ_B has also been reported [16], Which assumed all iron atoms possess the same magnetic moment, although the Al-rich quasicrystalline

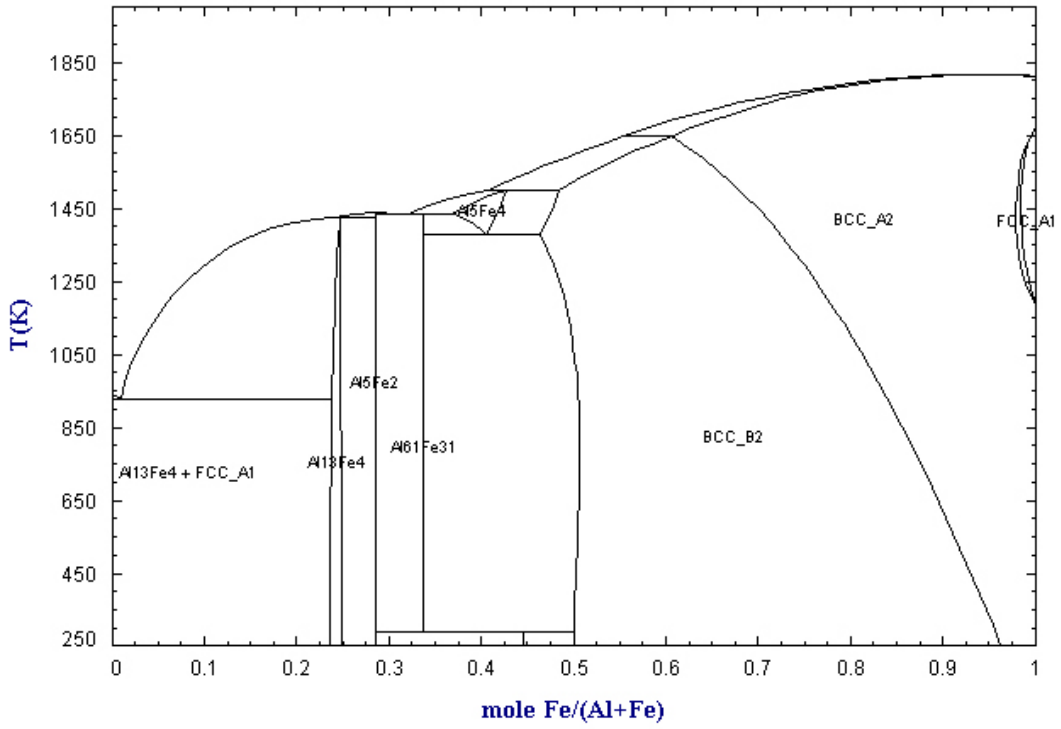

Fig. 1. Phase diagram of Fe-Al [18].

phases are more typically nonmagnetic [17].

Fe_2Al_5 has an orthorhombic structure (*Cmcm*, space group# 63) with 15.2(0.32) atoms per unit cell, shown in Fig. 3 [19]. There are 1 Fe site and 3 Al sites in the unit cell, of which 2 of the Al sites deviate considerably from full occupancy, with the occupation factors 0.36 and 0.23, and there is the possibility that Fe atoms can occupy these low-occupied sites. A three-dimensional framework is built up in Fe_2Al_5 with channels which have the shape of pentagonal antiprisms connected by side edges. There are two types of positions on the axes of the channels, both of which are occupied by the Al atoms. Since these positions are very close to each other, shorter

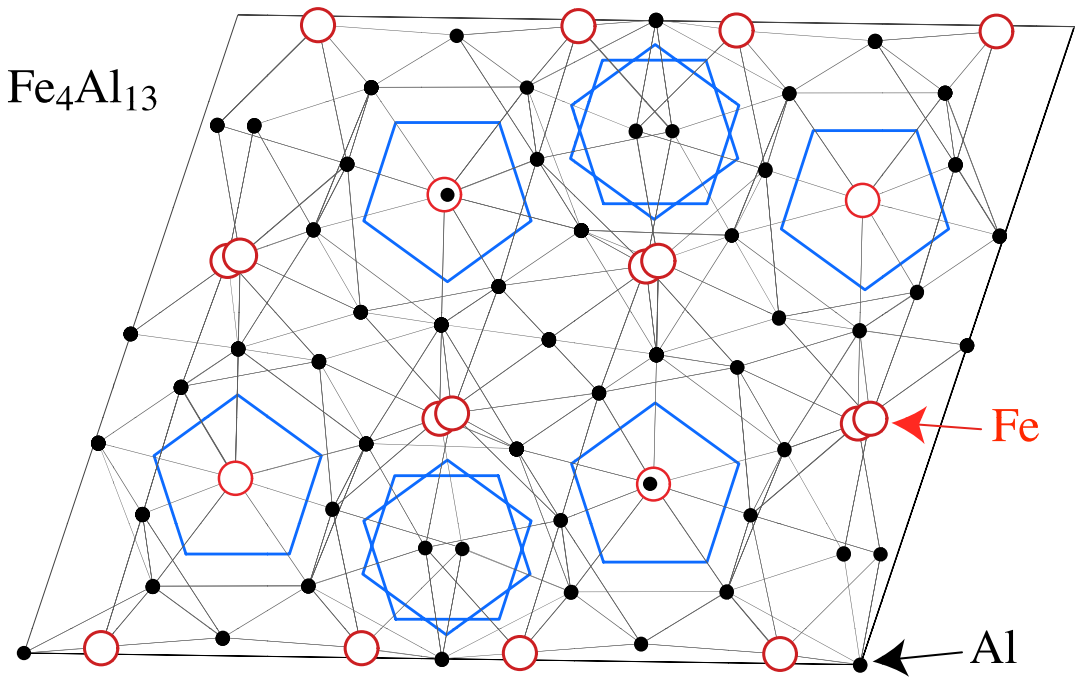

Fig. 2. Fe_4Al_{13} structure. Small filled circles: Al(78/unit cell); large open circles: Fe (24/unit cell). Two cells shown, viewed along the b axis. Inscribed pentagons indicate the pentagonal and decagonal channels identified by Grin, *et al.* [12], the latter composed of stacked pentagonal anti-prisms.

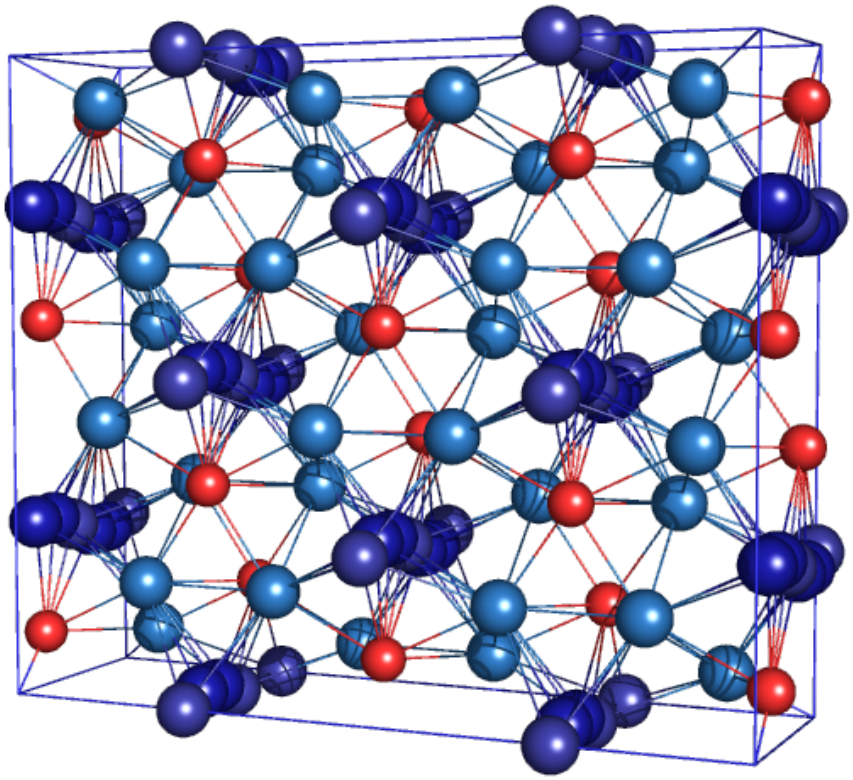

Fig. 3. Fe_2Al_5 structure: blue circles: Al(20 positions/unit cell); red circles: Fe(4/unit cell).

than the the sum of atomic radii, both of them can not be occupied at the same time and consequently the occupation of these sites is incomplete. According to the structural features, Fe_2Al_5 has been considered a quasicrystal approximant similar to Fe_4Al_{13}. Also a sizable magnetic moment, 0.77 μ_B per Fe, was observed [16].

$FeAl_2$ has a more complicated structure, a triclinic unit cell, shown in Fig. 4, as solved by Corby and Black [20]. This structure is a distorted close-packed configuration, with 18 atomic sites including 10 Al sites, 5 Fe sites, and 3 sites having mixed Al and Fe occupation. Despite the high coordination, the preference for Fe-Al bonding is apparent, with Fe-Al neighbors exhibiting the smallest bond lengths, indicating

the importance of Fe-Al hybridization, which can lead to a nonmagnetic configuration with a pseudogap to stabilize the structure. However, magnetic measurements showed that $FeAl_2$ exhibits a large effective local moment of 2.55 μ_B per Fe, indicating strong local-moment magnetism in this material. A susceptibility cusp at T_f = 35 K and frequency-dependent susceptibility below T_f were observed, corresponding to spin-glass behavior, which can be due to both frustration on the complex lattice structure and disorder from the occupation of the mixed sites [21]. And resistivity measurements showed a minimum near 35 K, which is attributed to the development of short-range spin correlations in the spin-glass phase. Furthermore a recent set of thermoelectric power (TEP) measurements indicated $FeAl_2$ to be a semimetallic with a pseudogap of about 0.1 - 0.2 eV, according to the slope of the TEP changes sign for $FeAl_2$ at around 100 K [22].

2. $Al_{20}V_2R$

$Al_{10}V$ is another interesting transitional-metal aluminide. It has a cubic structure containing 176 atoms, with 1 V site, 3 Al sites (Al_1(16d), Al_2(48f), Al_3(96g))and one void(8b), which can be partially occupied by Al extending the phase from $Al_{10}V$ to $Al_{10.5}V$ [23]. The void site is centered in an Al_{16} Frank-Kasper Friauf polyhedron, connected by a V-Al Kagomé network [24]. Al_1 and Al occupying the void site are not bonded directly to V atoms and have an unusually large distance to the neighbors, the most vibrational freedom and weakest bond energy. Due to loose packing of the atoms in positions which are not in contact with V atoms, $Al_{10}V$ has a large average atomic volume, 17 $Å^3$ per atom. Low-temperature specific-heat and electrical-resistivity measurements showed a local soft mode – Einstein model, associated with the loose Al atom occupying the large hole and rattling around with a low frequency in the structure [25].

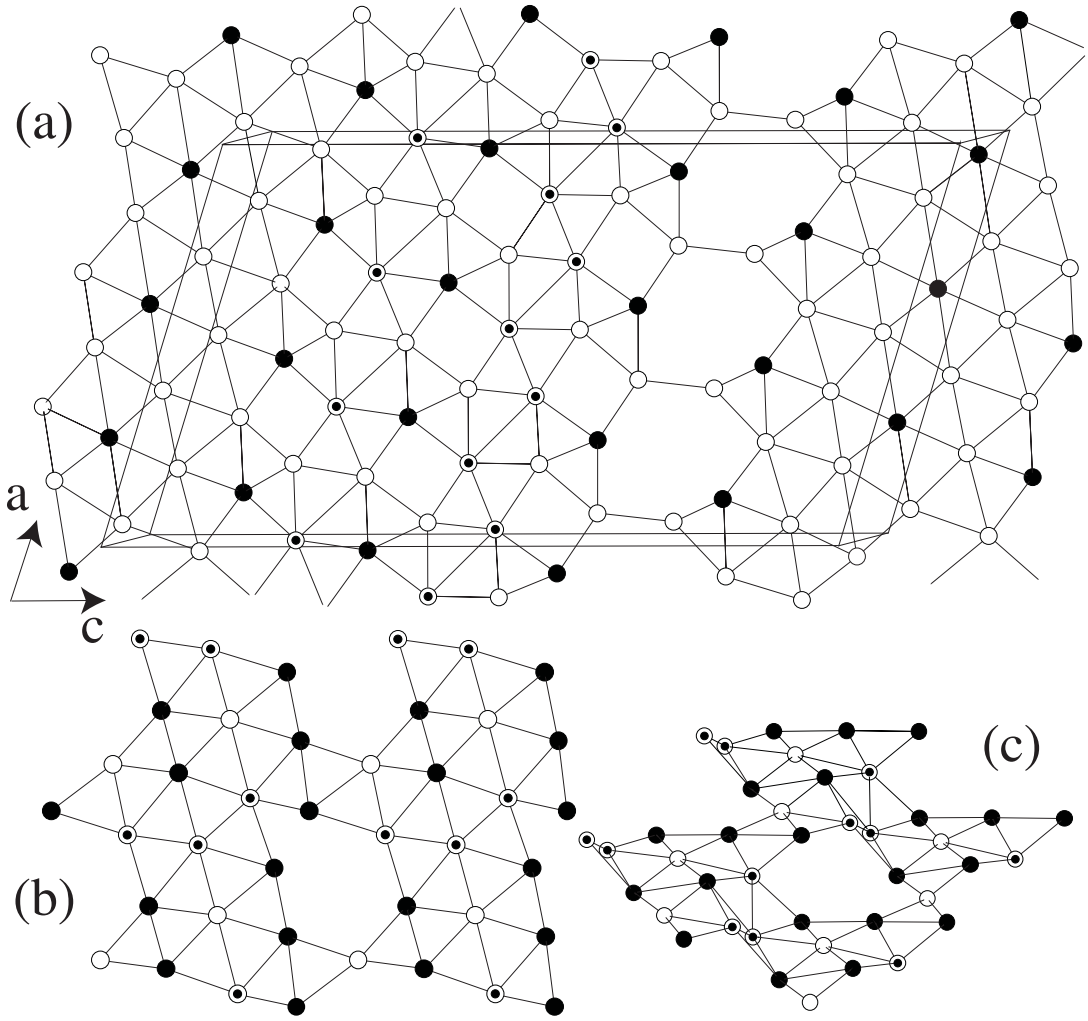

Fig. 4. $FeAl_2$ structure. Filled circles: Fe (5/cell); open circles: Al (10/cell); dot-filled circles: mixed-occupancy sites (3/cell). (a) (021) plane, with frame showing a 3×3 set of triclinic unit cells. (b) View along (101) showing Fe pairs/triads. This Fe-containing layer alternates with an Al-only layer. (c) Rotated view of layer pictured in (b).

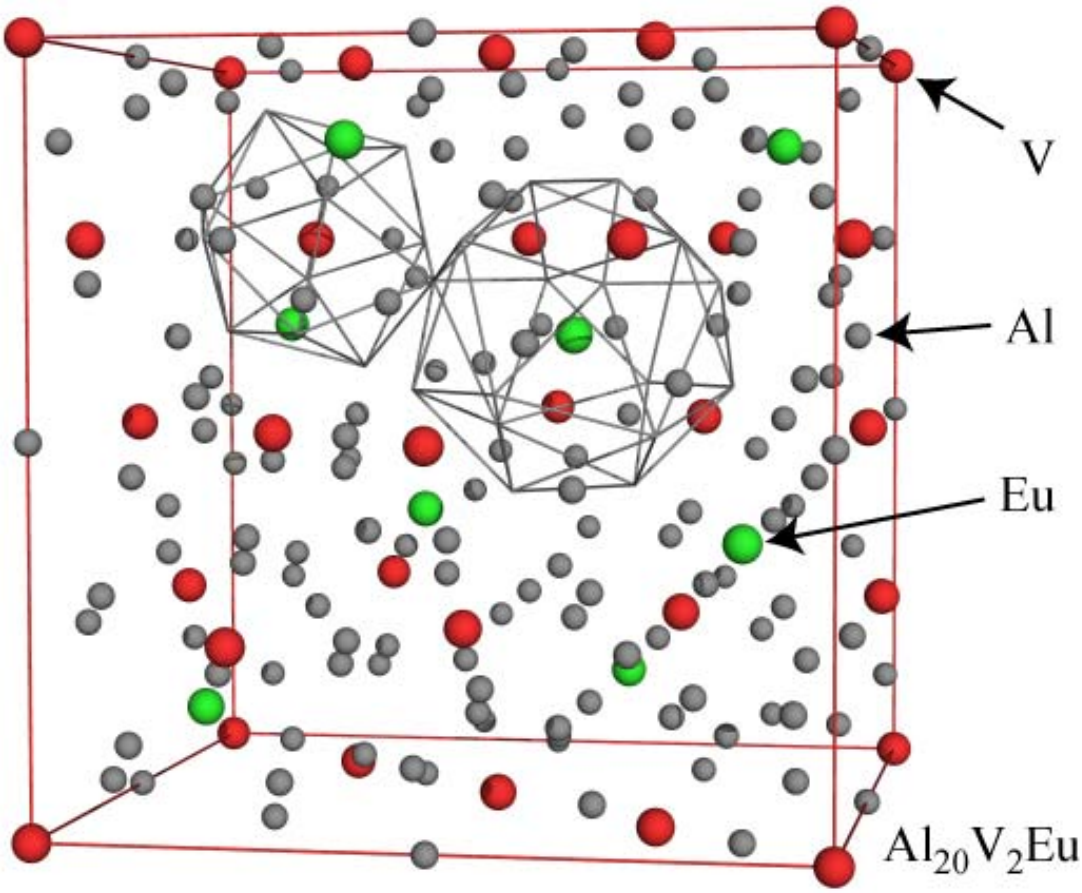

Fig. 5. Cubic $Al_{20}V_2Eu$ structure: Eu nested in Al_{16} Frank-Kasper Friauf polyhedra, connected by a V-Al Kagom network

Recently, it was shown the void inside the structure may be occupied not only by an Al atom but also by a rare-earth metal. There are 79 of these materials [27], plus Zn-based analogs which have been of recent interest [26]. $Al_{20}V_2Eu$ is one of the recently discovered $Al_{20}T_2R$ compounds, T=transition metal and R=rare earth [27]. The regularly-spaced R atoms in highly-symmetric cages and the quasicrystal-like framework makes these materials potentially of interest of their magnetic behavior.

3. Present Problem and This Study

While there is general agreement of pseudogap in the electronic structure of Al-rich transition-metal aluminides due to the strong sp-d coupling, most previous work focused on Al-Mn system. In Al-rich Fe-Al, a microscopic understanding of the electronics and magnetism of this system is still missing.

For Fe_4Al_{13} although band structure calculations showed there to be a low DOS at the Fermi level consistent with a pseudogap behavior [1], there is no direct evidence for the existence of such a pseudogap. Due to the 2 partially occupied Al sites in Fe_2Al_5, there is some difficulty in doing the theoretical electronic structure calculations and no further experimental investigation of this material was found. Also magnetism in Fe-Al system is worth more study; although susceptibility measurements showed Curie-Weiss behavior with local moments, a spin-glass at low temperatures in $FeAl_2$ and dilute-Fe in Al magnetism is not complete understood [28]. Also due to the potential practical applications (structural alloys, low-stick surfaces, etc.), further investigation will be helpful to gain more insight into the magnetic and electronic properties.

There has been more and more interest in intermetallic compounds containing rare-earth and transition metals, in cases of weak magnetic behavior resulting in variety of characteristics including spin and valence fluctuations, spin and charge orderings, heavy Fermion behavior and Kondo insulators. Kondo insulators are $3d$, $4f$ and $5f$ intermetallic compounds. At high temperatures, they behave like metals. But as temperature is reduced, an energy gap opens in the conduction band at the Fermi energy and the materials become insulating. The formation of the gap in Kondo insulators has been proposed to be a consequence of hybridization between the conduction band and the f-electron levels, giving a spin gap. Thus, metallic

behavior should be recovered when the gap is closed by external parameters.

Recent experiments on $Ce_3Bi_4Pt_3$[29], YbB_{12} [30], and SmB_6 [31] in high magnetic fields indicate closure of the Kondo-insulating gap, exemplifying a transition from the Kondo insulator to a correlated metal. This Kondo insulator to metal transition can also be induced by pressure and alloying, as observed in SmB_6 [32] and $FeSi_{1-x}Ge_x$ [33]. Some theoretical works showed a magnetic-field-induced transition in a Kondo insulator [34]. Although Eu is known to exhibit mixed-valence behavior, heavy-Fermion Eu compounds are very rare; one example is $EuCu_2(Ge_{0.3}Si_{0.7})$ showing $\gamma = 191$ mJ/K mol. $Al_{20}V_2Eu$ is one of the recently discovered $Al_{20}T_2R$ compounds, however there has been no further experimental study.

To clarify the physical nature of the Al-rich Fe-Al and $Al_{20}V_2Eu$ systems, we applied the nuclear magnetic resonance (NMR) technique which is a local probe providing valuable information regarding fundamental issues such as Fermi level features, formation of local moments, magnetic fluctuation and ordering, heavy-Fermion behavior, etc. In this work, we report the results of ^{27}Al NMR study of these aluminides between 4 and 500 K. Measurements of the spin-lattice relaxation rate, $1/T_1$, can provide information about the DOS around Fermi-level to determine the predicted pseudogap energy. Also the temperature dependence of $1/T_1$ will allow us to investigate the magnetic moments and the dynamics of the ordering process. Knight shifts measure the effective field at the nucleus and provide the information about the local interaction mechanism(contact, core polarization, orbital, etc.) between the nucleus and the corresponding contribution(*sp*-band, *d*-band, orbital, local magnetic electron, etc.) to the susceptibility χ. In addition to NMR, DC susceptibility, specific heat and transport measurements were carried on these alloys to study the magnetic and electronic properties.

CHAPTER II

NMR IN SOLIDS

NMR has been developed, since its discovery in the mid-1940s, into a highly sensitive and versatile tool. It covers an extremely broad range of applications reaching from pure nuclear physics to the newly introduced medical application, NMR imaging, including atomic physics, condensed-matter physics and chemistry, and biological and chemical analysis. Here I briefly review the basic concepts of NMR and the features related to the electronic and magnetic properties in condensed matter [35, 36].

A. Spin Hamiltonian

We consider a nucleus with a magnetic moment $\vec{\mu}$ and an angular momentum $\hbar\vec{I}$, the two quantities are parallel, and we can write

$$\vec{\mu} = \gamma_n \hbar \vec{I}, \tag{2.1}$$

where γ_n is the nuclear gyromagnetic ratio. The energy of interaction with the applied magnetic field $\vec{H}$ is -$\vec{\mu}\cdot\vec{H}$. If the field to be H_0 along the z-direction, then

$$U = -\mu_z H_0 = -\gamma_n \hbar I_z H_0. \tag{2.2}$$

The allowed values of I_z are m = -I, -I+1,..., -I, and U = -$m\gamma_n\hbar H_0$. Therefore the energy difference between two adjacent levels, called Zeeman energy, is

$$\Delta E = \hbar\omega_0 = \gamma_n \hbar H_0. \tag{2.3}$$

Here the resonance frequency ω_0 is called the Larmor frequency which does not depend on m. Nuclear magnetic resonance is a branch of spectroscopy to encompass all studies of the nature of the energy levels of material systems and of the transitions

induced between neighboring levels with the selection rule $\Delta m = \pm 1$ through an RF (radio-frequency) field applied to the sample with a frequency close to ω_0. Then the energy difference for the transitions of a nucleus is directly proportional to the applied magnetic field. However, the proportionality constant is different for different environments because the electrons in the solid respond differently to the applied field, causing an additional field, ΔH, at the resonating nucleus. This magnetic field at the nucleus, ΔH, is often referred to as the "hyperfine field".

There are several contributions to the interaction of a nucleus with electrons in a solid, and this interaction is called the hyperfine interaction. Using NMR technique, the hyperfine interaction can be extracted by means of Knight shift and spin-lattice relaxation rate measurements and thus reveal the electronic and magnetic properties of condensed matter. In metals, the major hyperfine interaction is the coupling between the magnetic moments of a nucleus and an electron. The Hamiltonian is

$$H = 2\frac{8\pi}{3}\mu_B\gamma_n\hbar\vec{I}\cdot\vec{S}\delta - 2\mu_B\gamma_n\hbar\vec{I}\cdot[\frac{\vec{S}}{r^3} - \frac{3\vec{r}(\vec{S}\cdot\vec{r})}{r^5}] - \gamma_n\hbar\frac{e}{mc}[\vec{I}\cdot\frac{(\vec{r}\times\vec{p})}{r^3}], \qquad (2.4)$$

where μ_B is the Bohr magneton, γ_n is the magnetogyric ratio, $\vec{I}$ and $\vec{S}$ are the nuclear spin and electron spin, respectively, $\vec{r}$ is the radius vector of the electron with the nucleus at the origin, and the other symbols have their usual meaning. The first term is the Fermi contact interaction term, where s-wave functions describe the major part of the conduction electrons. The second term represents the spin dipolar interaction between nuclear and electron spins. The third term represents the interaction of the nuclear spin with the orbital motion of the electrons.

B. Knight Shift

At a fixed applied magnetic field, the resonance frequency of the nuclear spin in a sample is observed at a position with a slight shift compared to that of a paramagnetic salt. This shift is called a Knight shift. The Knight Shift, K, measures the hyperfine field at the nucleus produced by those electrons in a metal which respond linearly to an applied field, H_{appl}, and is available as a tool for the study of electronic and magnetic properties in materials. The Knight shift is a sum of terms corresponding to local interaction mechanisms (contact, core polarization, orbital, etc.) between the nucleus and the corresponding contribution (sp-band, d-band, orbital, etc.) to the susceptibility χ.

The source of Knight shift first used to interpret shifts in simple metals was the Fermi contact interaction between the resonating nucleus and the s-electrons. According to the theory,

$$K = \frac{8\pi}{3}\chi_P\langle|\Psi_s(0)|^2\rangle_{FS} = \frac{8\pi}{3}\chi_P P_F, \tag{2.5}$$

where χ_P is the pauli paramagnetic spin susceptibility per atom, and $\langle|\psi_s(0)|^2\rangle_{FS}$, often denoted as P_F, is the square of the s-wave function at the nucleus averaged over those electrons at the Fermi surface (FS). By definition:

$$\langle A\rangle \equiv \frac{8\pi}{3}\langle|\Psi_s(0)|^2\rangle_{FS} = \frac{8\pi}{3}P_F, \tag{2.6}$$

$\langle A\rangle$ represents the hyperfine field, $H_{eff} = \mu_B\langle A\rangle$. With this definition, Eq. (2.6) becomes

$$K = \langle A\rangle\chi_P. \tag{2.7}$$

This contact Knight shift from the Pauli susceptibility thus is denoted as K_s,

$$K_s = \frac{H_{hf}}{\mu_B}\chi_P. \tag{2.8}$$

From the free electron model, the Pauli susceptibility χ_P is

$$\chi_P = \mu_B^2 g(E_F), \tag{2.9}$$

where $g(E_F)$ is the electronic DOS at the Fermi surface. Thus if the hyperfine field is known, the Knight shift can be used to determine $g(E_F)$.

The induced Pauli paramagnetism interacts directly with the nucleus through the contact and spin-dipolar interactions, while the shift from core polarization effects, termed the core polarization Knight shift (K_{core}), is indirect. Due to the Pauli exclusion principle, valence electrons may polarize the closed shell of an ion core and the paired electrons in the conduction bands below the Fermi surface, E_F, producing spin densities which will then interact with the nucleus through the contact interactions and only the spin polarization of closed s-shells and of the s-character in the conduction bands below E_F will interact directly with the nucleus. These interactions arise from differences induced in the spatial behavior of spin up and down pairs of electrons with zero net spin induced in the electrons. Estimates of the core polarization are negative for d- and f-shells, implying a core spin density at the nucleus whose orientation is antiparallel to the unpaired spin responsible for the polarization and leading to a possibly negative Knight shift. In contrast, the core polarization response to an unpaired s-valence electron is always positive and simply serves to enhance the contact interaction associated with the valence electron.

Besides these contributions to the Knight shift coming from the Pauli paramagnetism of the conduction electrons, there is a contribution from the orbital magnetic moment of the conduction electrons induced by the applied magnetic field. In analogy

with Eq. (2.7),

$$K = \langle b \rangle \chi_{orb}, \tag{2.10}$$

where $\langle b \rangle$ is an appropriate orbital hyperfine coupling constant. In contrast to the Pauli contribution, the orbit contribution is not proportional to $g(E_F)$. The orbital Knight shift involves the orbital moment induced in occupied conduction electron states by an applied magnetic field. Application of a magnetic field to the occupied and unoccupied Bloch states causes an admixture which produces a moment interacting with the nucleus. And there is little or no temperature dependence to this term, in analogy to Van Vleck temperature-independent paramagnetism in ionic salts. A rough estimate of the strength of the orbital Knight shift is given by

$$K_{orb} \approx \frac{n_i n_f \langle \frac{1}{r^3} \rangle}{\Delta}, \tag{2.11}$$

where $\langle \frac{1}{r^3} \rangle$ is the average of $\frac{1}{r^3}$, n_i and n_f are the numbers of occupied and unoccupied Bloch states respectively and Δ is the conduction electron band width. According this equation, a small Δ will cause a considerable orbital shift which can be very important in transition metals because Δ is usually small in d bands.

Besides the Knight shift, there are other sources of magnetism that contribute to the NMR line shifts. If the material possesses local magnetic electrons, a strong $1/T$ dependence is likely to be present, resulting from the local electron-conduction electron (RKKY) interaction which causes an enhancement of the Pauli contact term.

From the discussion above, the observed K can be a sum of these terms as follows:

$$K = K_s + K_{orb} + K_{core} + K_{loc}(T). \tag{2.12}$$

The NMR line shift is thus an important tool to probe hyperfine interactions of various types, and separate the spin susceptibility into different mechanisms.

C. Line Shape

The NMR line shape depends on several different factors. The NMR line shape has a certain width owing to the spread of Larmor frequencies in an inhomogeneous magnetic field. The electron-nuclear dipole interaction will result in anisotropic Knight shifts and cause a line broadening. Besides, there is a quadrupole effect in a non-cubic environment for nuclei with spin $> 1/2$, which will affect the NMR transitions and the presence of impurities in diluted crystals will cause the NMR line broadening via dipolar couplings.

D. Spin-lattice Relaxation Rates

Considering a system of N nuclear spins, the distribution of nuclei among the energy levels is given by the Boltzmann factor. When this equilibrium is disrupted (e.g., by rf power), the nuclear spin system returns to equilibrium with the lattice by a relaxation process characterized by a time T_1, called the spin-lattice relaxation time. Thus T_1 measurements can reveal the dynamical behavior of the hyperfine interactions.

In a metal, the nuclear relaxation is produced by their coupling to the spin magnetic moments of the conduction electrons. The dominant mechanism is the magnetic part of hyperfine interaction. There are several terms involved in this interaction, including contact, orbital and dipolar relaxation rates.

Any nuclear relaxation is accomplished by transition between spin states. Such transition rate is a sum over all electron states able to participate in the relaxation process. Considering nuclear spins at high applied magnetic field, we assume that the electron relaxation is sufficiently short and the temperature is high for the electronic Zeeman Energy to be much smaller than $k_B T$. Under these assumptions, electrons

with spins up or down have approximately the same Fermi distribution function

$$f(E) = \frac{1}{1 + exp(E\text{-}E_F)/k_B T}. \tag{2.13}$$

The probability of an electron making a transition from a state of kinetic energy E to state of energy E' must be weighted by the factor $f(E)[1 - f(E')]$, which is the simultaneous probability for the initial state to be occupied and for the final state to be empty prior to the transition. According to the nucleus-electron interaction $\langle i|V_{n-e}|f\rangle$ (Eq. (2.4), the spin lattice relaxation rate should be expressed as

$$\frac{1}{T_1} \propto \int \langle i|V_{n-e}|f\rangle^2 g^2(E) f(E)(1 - f(E))dE, \tag{2.14}$$

which $g(E)$ is the electronic density of states. If the transition involves a simultaneous electron-nuclear spin flip, the change in kinetic energy being very small, $f(E)[1 - f(E')]$ may be replaced by $k_B T\delta(E - E_F)$. Thus $1/T_1$ will be proportional to temperature, a phenomenon known as Korringa behavior and the relaxation measurement can probe the electronic properties, such as the DOS structure around the Fermi level.

In non-metallic solids, the effective nuclear Hamiltonian is

$$H_n = \gamma_n \hbar \vec{I} \cdot \vec{H}_0 + \vec{I} \cdot [A] \cdot \langle \vec{S} \rangle, \tag{2.15}$$

where A is the transfer hyperfine energy and $\langle \vec{S} \rangle$ is the average value of the electronic spin, averaged due to the shorter electron spin fluctuation time compared with the nuclear Larmor period. The strength of typical electron-nuclear interactions $(A/\gamma_n \hbar)$ varies between 10^3 and 10^7 Oe. In a concentrated paramagnetic crystal, exchange interactions between electron spins may greatly decrease the electronic fluctuation

time. For nearest neighbor interactions (J), we find an exchange frequency

$$\omega_E = [8J^2 z S(S+1)/3\hbar^2]^{\frac{1}{2}}, \tag{2.16}$$

where J is the interaction strength, z denotes the number of nearest neighbors which are exchange coupled to a given spin. By the calculation of the transition probability with perturbation theory, we obtain

$$T_1^{-1} = (2\pi)^{\frac{1}{2}}(A/\hbar)^2(3\omega_E)^{-1}S(S+1), \tag{2.17}$$

which is temperature-independent.

In non-metallic solids with some paramagnetic impurities, the electron spin fluctuation time is not sufficiently short, the expression is

$$T_1^{-1} = 4\pi N b D, \tag{2.18}$$

where N is the concentration of paramagnetic centers in the sample and D is the diffusion constant for nuclear spin magnetization transfer. D is of the order Wa^2, where a is the neighbor distance and W the probability of a flip-flop between nearest neighbors. The coefficient b depends on whether the electronic fluctuations are slow or fast with respect to the nuclear Larmor frequency, ω_n. The electron relaxation time τ is usually in the fast motion limit with respect to ω_n, and b is proportional to $\tau^{1/4}$. In diluted paramagnets, where interaction between the electronic moments is negligible, τ normally does not exhibit a pronounced temperature dependence, so that the paramagnetic relaxation rate of Eq. (2.18) can reasonably be approximated to be temperature-independent.

CHAPTER III

BASIC THEORY OF NMR

A. Motion of Free Spins

A basic problem in nuclear magnetism is the description of the behavior of a free spin in a uniform magnetic field. A free spin is a system with an angular momentum $\vec{L}$ and a magnetic moment $\vec{M} = \gamma\hbar\vec{I}$. In the static magnetic field, $\vec{H}$ will produce a torque $\vec{M} \times \vec{H}$, equal to the rate of change $\hbar(d\vec{I}/dt)$ of its angular momentum. Thus the equation of motion is

$$\frac{d\vec{M}}{dt} = \gamma_n \vec{M} \times \vec{H}. \tag{3.1}$$

Therefore the torque causes $\vec{M}$ to precess about the the field at an angular frequency $\omega_0 = \gamma_n H_0$. Viewed from the laboratory frame, Eq. (3.1) is replaced by the Bloch equations:

$$\frac{dM_x}{dt} = \gamma_n(\vec{M} \times \vec{H})_x - \frac{M_x}{T_2}, \tag{3.2}$$

$$\frac{dM_y}{dt} = \gamma_n(\vec{M} \times \vec{H})_y - \vec{M}_y T_2, \tag{3.3}$$

$$\frac{dM_z}{dt} = \gamma_n(\vec{M} \times \vec{H})_z - \frac{M_z - M_0}{T_1}, \tag{3.4}$$

where M_0 is the equilibrium magnetization of a sample in an external field which we assume to be along the z-axis. T_1 and T_2 are longitudinal and transverse relaxation times. As mentioned in Chapter II, the spin-lattice relaxation is responsible for T_1, and the local field from neighboring nuclei at each nuclear site is responsible for T_2.

A rotating frame with respect to the laboratory frame with an angular velocity about the external magnetic field is in the same direction in which nuclear spins precess. According to the general law of of relative motion, the time derivative in the laboratory frame, and its partial derivative computed in the rotating frame are

related through

$$(\frac{d\vec{M}}{dt})_{lab} = (\frac{\partial\vec{M}}{\partial t})_{rot} + \vec{\omega} \times \vec{M}. \tag{3.5}$$

Combining Eq. (3.1) and Eq. (3.5), the motion of the magnetic moment in the rotating frame is given by the equation

$$(\frac{\partial\vec{M}}{\partial t})_{rot} = \gamma_n \vec{M} \times (\vec{H} + \frac{\vec{\omega}}{\gamma_n}). \tag{3.6}$$

This has the same form as Eq. (3.1) provided the magnetic field is replaced by an effective field $\vec{H}_{eff} = \vec{H} + \frac{\vec{\omega}}{\gamma_n}$, seen by the magnetization in the rotating frame. If the rotating frame has an angular frequency equal to $-\gamma_n\vec{H}$, the effective field $\vec{H}_{eff}$ vanishes, and $\vec{M}$ is invariant with time in the rotating frame.

For pulsed NMR, a rotating field $\vec{H}_1$ with an angular frequency $\vec{\omega}$ with respect to the laboratory frame is also applied perpendicular to the static field $\vec{H}_0$. Thus the effective field in the rotating frame can be written as $\vec{H}_{eff} = \vec{H}_0 + \frac{\vec{\omega}}{\gamma_n} + \vec{H}_1$. At resonance the external field cancels ω/γ_n and leaves only $\vec{H}_1$. Since $\vec{H}_1$ rotates at the same frequency as the frame, the angular precession frequency about $\vec{H}_1$ is $\gamma_n H_1$ and in a time period t, the angle θ through which M precesses is

$$\theta = \gamma_n H_1 t. \tag{3.7}$$

B. FID and Spin-Echo

In pulse NMR experiment, a radio frequency (rf) magnetic field perpendicular to the static field is generated in a coil to excite simultaneously all nuclei whose resonance frequency is near the pulse frequency. After the rf field $\vec{H}_1$ is turned off, the signal induced in the coil is a free precession signal and, owing to its decay, is called a free induction decay (FID), which is modulated by the frequency of all nuclei excited by the pulse. The decay of the magnetization in the x-y plane can be exponential with

the time constant $T_2^\star$. $T_2^\star$ is approximately

$$\frac{1}{T_2^\star} = \frac{1}{T_2} + \gamma_n \Delta H_0, \tag{3.8}$$

where T_2 is from dipolar processes and ΔH_0 is the applied magnetic field inhomogeneity, since nuclei in the different parts of the field precess at slightly different frequencies, hence quickly get out of phase with each other. And the magnetization decayed in the rotating x-y plane due to the external field inhomogeneity can be refocussed into an echo by an appropriate pulse. This is called spin echo.

We usually use Hahn echo sequence in the NMR measurements. This is a two-pulse sequence, the first one 90° and the second one, turned on a time τ later, a 180° pulse. In the rotating frame, at t = 0, the magnetization is in thermal equilibrium lying along the z direction. After the first 90° pulse on the x-axis, which produces a rotation of $\theta = 90°$ according to Eq. (3.7), the magnetization immediately rotates to be the $-y$ direction. Due to the field inhomogeneity, the total magnetization vector is the sum of smaller magnetization vectors each arising from a small volume experiencing a homogeneous field and each of these components of the magnetization will precess with its own characteristic Larmor frequency. As a result, the different contributions of the magnetization will get out of phase with each other. At time τ, a fractional magnetization δM has precessed an extra phase either positive or negative. Then the 180° pulse is applied and the magnetization is flipped to the $+y$ direction. δM will again advance through the same phase, which will bring the magnetization refocus along the + y-axis at t = 2τ. Therefore, at time 2τ after the first pulse, a FID-type signal termed a spin echo will be discovered. The spin echo consists of two FID's back-to-back. The echo amplitude may diminish exponentially with a time constant T_2 as τ varies.

C. Measurement of Spin-Lattice Relaxation

To measure the spin-lattice relaxation rate with the spin-echo technique, a third pulse is placed at a time τ_{wait} before the 90° - τ - 180° sequence. The third pulse tips M to the $-z$ direction in the rotating frame. The spin systems return to equilibrium with the characteristic time T_1. The spin-echo amplitude thus depends on the time τ_{wait}. And by repeating such a spin-echo sequence with different τ_{wait}, a magnetization recovery curve can be constructed to reveal the value of T_1.

For a nucleus in a high static magnetic field, the magnetization of the central transition is directly proportional to the population difference between $I = 1/2$ and -1/2. For any nucleus with $I \neq 1/2$, according the echo-spin sequence to measure the spin-lattice relaxation rate, the relaxation will follow a multiexponential recovery curve with the time constant T_1. Taking $I = 5/2$ for example, the magnetization recover curve is following[37]

$$\frac{M(t)}{M(0)} = 0.0286e^{-\frac{\tau_{wait}}{T_1}} + 0.178e^{-\frac{6\tau_{wait}}{T_1}} + 0.793e^{-\frac{15\tau_{wait}}{T_1}}. \tag{3.9}$$

By fitting to such multiexponential functions, we can find the T_1.

CHAPTER IV

EXPERIMENTAL APPARATUS

The major instruments required in my experiments include the NMR spectrometer, superconducting quantum interference device (SQUID), and physical property measurement system (PPMS).

A. NMR Spectrometer

The major components of the NMR experimental apparatus are a pulsed spectrometer, a 9 T superconducting magnet, and two temperature controlled probes, one for 4 K to 300 K, another 300 K to 500 K. The pulsed spectrometer built by Prof. Ross is a combination of the transmitter, responsible for the application of the RF pulse, and the receiver, the detection of the sample's response.

The probe is a key component of the spectrometer. It contains the sample within the magnet and provides the necessary hardware to measure the sample temperature. Also it couples the sample to the transmitter and the receiver in order to permit the excitation and detection of an NMR signal. The circuit of the probe is basically a tunable LC circuit. The sample coil is the inductor, a simple device selecting from a non-magnetic good conductor and containing no element which possess resonance frequencies close to the sample signal. Copper was used in my experiment to measure signal of Al. The capacitors have to be variable and also non-magnetic. Besides, my NMR experiments require the capacitors to have a wide operation temperature range and to be moved freely at very low temperatures.

To perform the experiment in a wide temperature range, I used two different probes with the ability to achieve desired temperature. The probe circuit is placed in a copper cylindrical shell. Two thermometers are employed to sense the temperature,

including a thermocouple for temperature above 77 K and a calibrated thin-film chip resistance thermometer for temperature below 77 K. Both sensors are non-magnetic and have little error in a high magnetic field. A commercial heater wire made of Cu-Ni alloy of about 10 Ω was twisted and wound around the copper shell.

To perform measurements between 77 K and 300 K, LN_2 is filled in a LN_2 reservoir which provides the isolation between the magnet and the probe. The samples are cooled to the surrounds by radiation down to nearly 80 K. The electrical current provides power to the resistance heater to achieve the desired temperature. Liquid helium is used for the measurement between 4 K and 77 K. We transfer LHe directly to the dewer for 4 K measurement, and apply a small current to the heater to the set temperature.

B. SQUID and PPMS

The SQUID is a system to measure the magnetic properties of a material sample over a temperature range from 1.8 K to a couple of hundreds degrees above room temperatures at different magnetic fields. The PPMS also has a variable temperature-field system, designed to perform a variety of automated measurements, including transport, specific heat, etc.

CHAPTER V

EXPERIMENTAL RESULTS AND DISCUSSIONS

This section will describe the methods of sample preparation, the measurement techniques, the data analysis and the discussions. Each sample was synthesized by arc melting the elemental constituents under argon, followed by further annealing in vacuum. The powder sample mixed with KBr of appropriate size was placed in a plastic vial for 4-300 K NMR measurements, while we put the specimen in a quartz tube for high temperature measurements. Both sample holders showed no observable ^{27}Al NMR signals. NMR experiments were performed at fixed field using a 9-T home-built pulse spectrometer. ^{27}Al NMR spectra were detected at approximately 98 MHz in constant field. In order to get the strongest signal, we optimized the 90° pulse duration. The Knight shift is determined by

$$K \equiv \frac{\upsilon_0 - \upsilon_R}{\upsilon_R} \times 100\%. \tag{5.1}$$

The observed υ_0 for ^{27}Al is obtained from the peak position of the spectrum. The reference, υ_R, for ^{27}Al Knight shift was the ^{27}Al resonance frequency of an aqueous $AlCl_3$ solution. Spin-lattice relaxation times (T_1's) were measured using the inversion recovery method. We recorded the signal strength by integrating the spin echo FFT of the ^{27}Al lines. For the recovery of the -1/2 $\longleftrightarrow$ +1/2 central transition, the T_1's were extracted by fitting to multiexponential curves [37] for $I = 5/2$ ^{27}Al, with T_1 as a parameter.

A. $FeAl_2$

1. Sample Preparation and Structure Analysis

The $FeAl_2$ sample was a different sample than that used in the previous study in this laboratory [21], however the spin-glass freezing temperature was found to be identical. The sample was characterized by powder x-ray diffraction (Bruker D8 Advance) using Cu K_α radiation. Structural refinement was carried out using the GSAS software package [38, 39].

X-ray diffraction results are shown in Fig. 6. The analysis showed no evidence for a second phase. Atomic occupation parameters are in reasonable agreement with the atomic weights reported earlier [20], though the refinement indicated Al occupation on Fe sites as well as mixed sites (up to 0.29 relative Al occupation of Fe site $1'$ [site labeling convention of Ref. [20]]). No Fe occupation of Al sites was found, and the mixed sites had Al occupation parameters in the range 0.36-0.53. The fit yielded $a =$ 0.4868 nm, $b = 0.6454$ nm, $c = 0.8796$ nm, $\alpha = 91.76°$, $\beta = 73.35°$ and $\gamma = 96.90°$, for the triclinic unit cell, with R values R_{wp}=0.0599 and R_p=0.0455. The Al/Fe ratio resulting from the refinement was 2.03.

Using the occupation parameters thus obtained, we calculated mean atomic coordination numbers, including partially occupied sites. This gave 2.5 Fe neighbors per Fe atom, and 3.5 Fe neighbors per Al atom. For this calculation, neighbors were assumed to be those at a distance less than 0.3 nm.

2. NMR Measurements

Fig. 7 shows ^{27}Al NMR spectra recorded between 4 K and 468 K, using a standard $\pi/2 - \tau - \pi$ spin-echo sequence. From the NMR pulse-length dependence, we find that the observed spectra correspond to 1/2 to $-1/2$ transitions for the $I = 5/2$

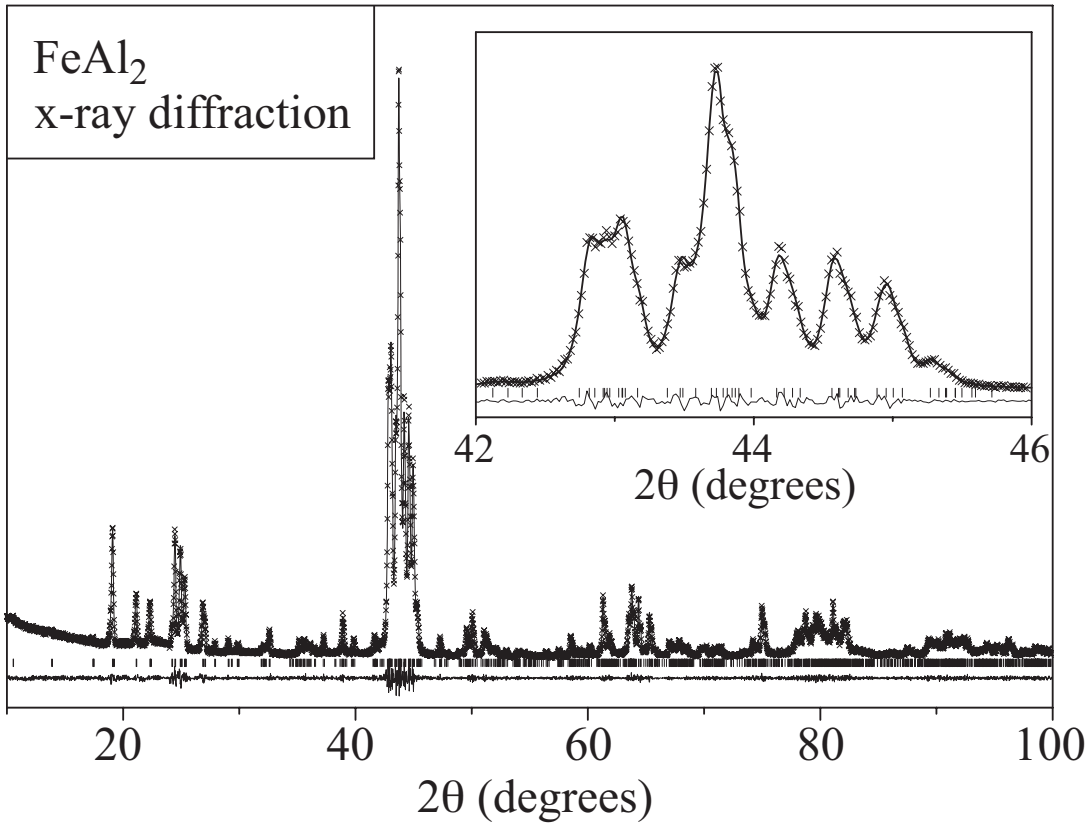

Fig. 6. Powder x-ray results for $FeAl_2$, with results of refinement and difference plot. Vertical marks are fitted reflections.

^{27}Al nucleus, implying that the other transitions are suppressed due to quadrupole broadening. Fig. 8 shows the relative shift obtained from the center of mass of these peaks. The shifts can be expressed by

$$K = K_1 + K_2(T). \tag{5.2}$$

A Curie-Weiss-type fit for K_2 (T) is shown by the dashed curve in Fig. 8, yielding $K_1 = -0.155$ %, with the Weiss temperature fixed at $\theta = -38$ K according to the susceptibility [21]. The 4 K point was excluded from this fit since it is below T_f. (Allowing θ to vary yielded an optimized value $\theta = -33$ K, with a large error bar of 15 K indicating insensitivity to that parameter.) The results correspond to ^{27}Al directly coupled to neighboring Fe moments, with a negative transfer hyperfine coupling. Note that the ^{27}Al shift does not increase relative to the Curie-Weiss curve below T_f as would be expected in the case of cluster-glass behavior, for which local ferromagnetic couplings should guarantee spin saturation in the large applied NMR field.

The transfer hyperfine coupling can be obtained from $K_2(T)$ [Eq. (5.2)] and the Fe moment calculated using $p_{eff} = 2.55$ and $\theta = -38$ K. This is shown in Fig. 9, where the moment per Al was obtained from $K_2(T)$ using $\mu_o H_{hf} = 190$ T as the Al s-spin hyperfine field [40]. From the least-squares slope we obtain a net Al hyperfine field of 1.2 T per μ_B on Fe. Dividing by 3.5, the mean Al-Fe coordination number, yields $\mu_o H_{hf}^{tr} = 0.35$ T per μ_B per Fe neighbor. A similar value of 0.24 T was found in Al_3V [41], while for dilute Al in Fe, the ^{27}Al shift [42] corresponds to $\mu_o H_{hf}^{tr} = 0.31$ T. (The latter is obtained from the quoted shift [42] by dividing by 2.2 μ_B and the coordination number, 8 for BCC Fe.) Thus the $FeAl_2$ couplings are not particularly large despite the anomalous Fe moment.

The negative $K_1 = -0.155$ % implies an Al spin polarization opposing that of the Fe d-orbitals, and in aluminides such behavior is observed in systems with

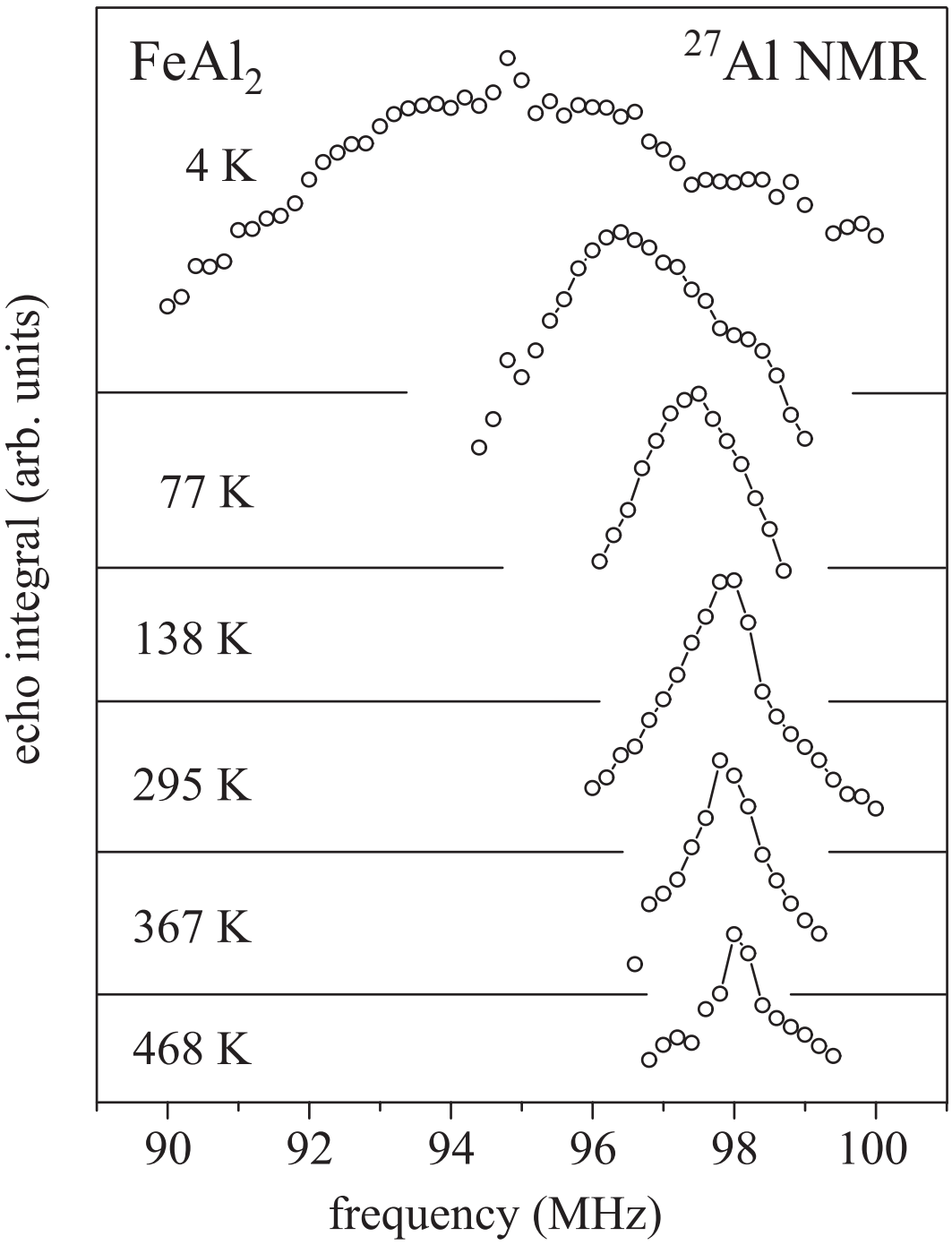

Fig. 7. ^{27}Al NMR spectra for $FeAl_2$. Data offset vertically for clarity.

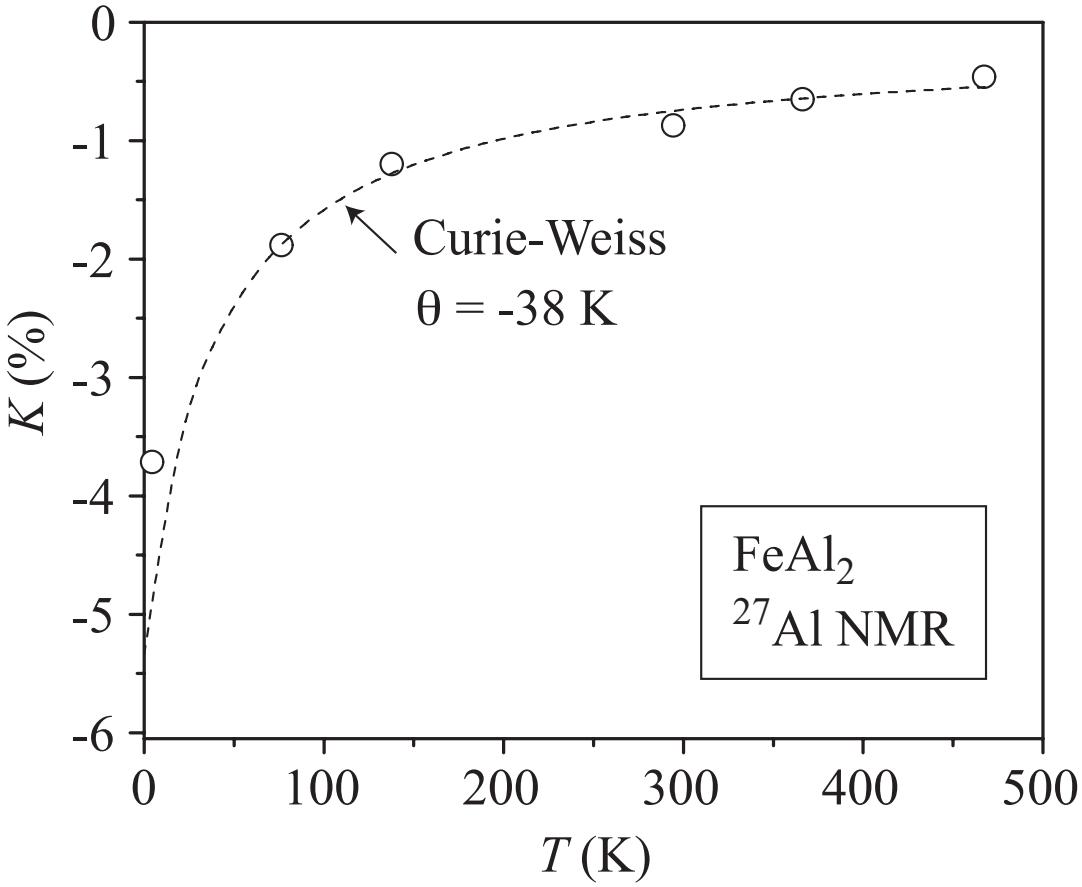

Fig. 8. ^{27}Al center-of-mass NMR shifts vs. temperature. Dashed curve: Curie-Weiss fit with $\theta = -38$ K.

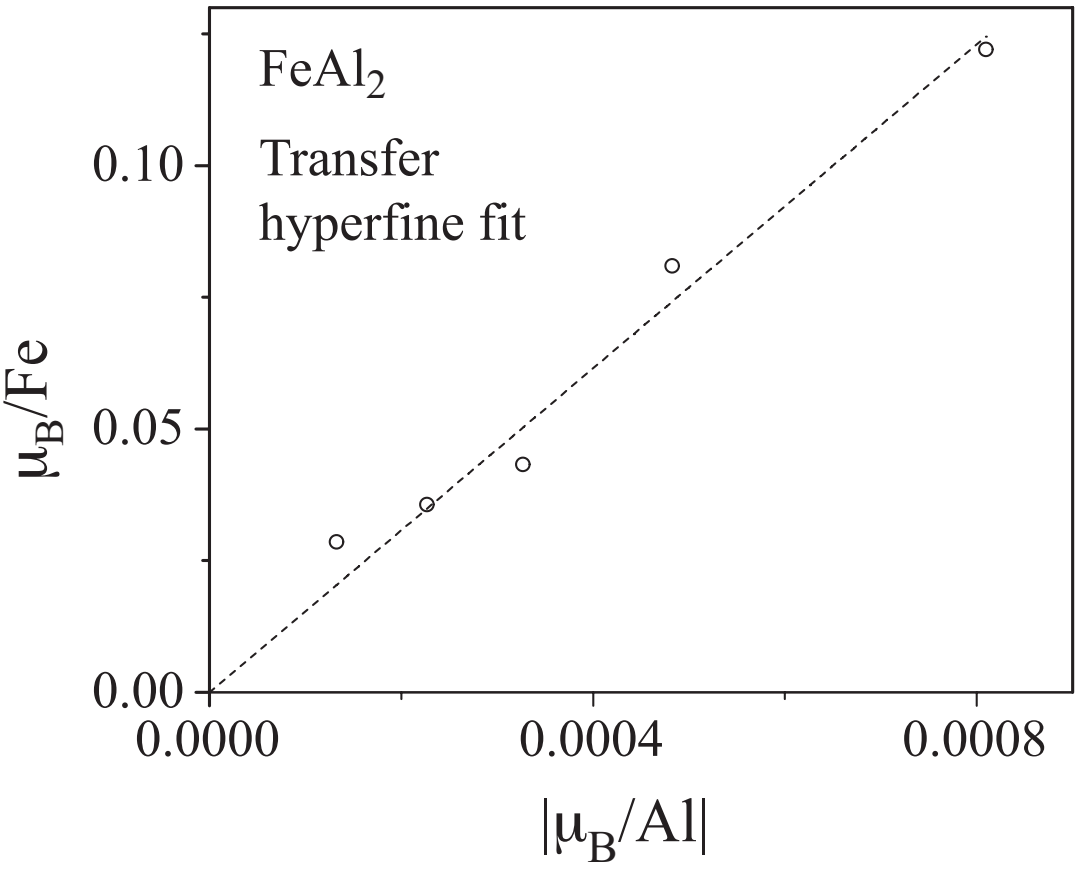

Fig. 9. $FeAl_2$ paramagnetic moment per Fe obtained from the magnetization curve, plotted vs. magnitude of effective on-site Al moment obtained from the mean NMR shift. Dashed curve is a least-squares linear fit.

open d shells: in nonmagnetic FeAl [43] and for a magnetic decagonal Al-Pd-Mn quasicrystal [44], values between -0.3 % and -0.6 % have been reported. Since this term is temperature-independent, it implies a Pauli susceptibility, and a predominant Fe d contribution to the Fermi surface. This contrasts the semiconducting behavior calculated for $FeAl_2$ in simpler geometries [45, 46].

The full width at half-maximum of the NMR line is plotted in Fig. 10, along with a fitted curve proportional to $1/(T-\theta)$, plus a T-independent background term. To see whether statistical occupation of Fe and mixed sites alone could account for this, we performed a Monte-Carlo-type calculation assuming Fe having identical paramagnetic moments, $H_{hf}^{tr} = 0.35$ T for all neighbors, and statistical site occupation according to the x-ray occupation parameters. The electron-nuclear dipole interaction resulting Curie-Weiss contribution to the linewidth was smaller than observed by a factor 1/3. Local variations in transfer couplings and/or moments (RKKY, etc.) may account for this difference, thus the observed widths appear reasonable.

The spin-lattice relaxation rate (T_1^{-1}) was measured by inversion recovery, irradiating the central portion of the ^{27}Al line, and using the integral of the spin echo. T_1 was extracted by fitting to multiexponential curves for magnetic relaxation of a $I = 5/2$ ^{27}Al central transition. Fig. 11 shows the results. At low temperatures, several peaks are observed, while at high temperatures the spin-relaxation rate is nearly constant with a value of 0.3 ms^{-1} (dashed line). These data resulted from two separate runs, showing consistent behavior.

The lowest-temperature peak in T_1^{-1} appears at 35 K, due to the slowing down of magnetic spins at T_f, as observed in other spin glass systems [47]. The maxima in T_1^{-1} above T_f do not correspond to observed features in magnetization [21] or specific heat [22]. These features are reminiscent of the behavior of AlPdMn quasicrystals [44, 48] for which multiple T_1^{-1} peaks are also seen. For that case, there is a reduction of Mn

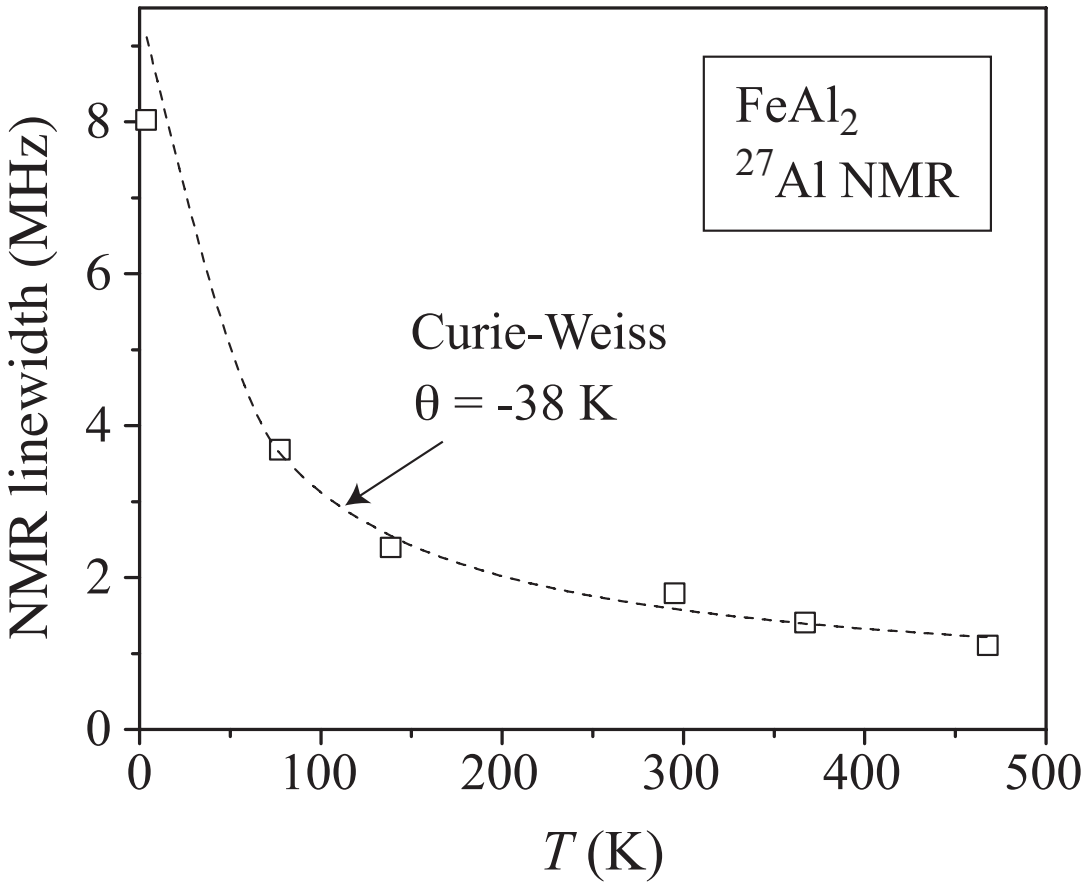

Fig. 10. ^{27}Al NMR FWHM linewidths for $FeAl_2$. Dashed curve is a Curie-Weiss fit with $\theta = -38$ K.

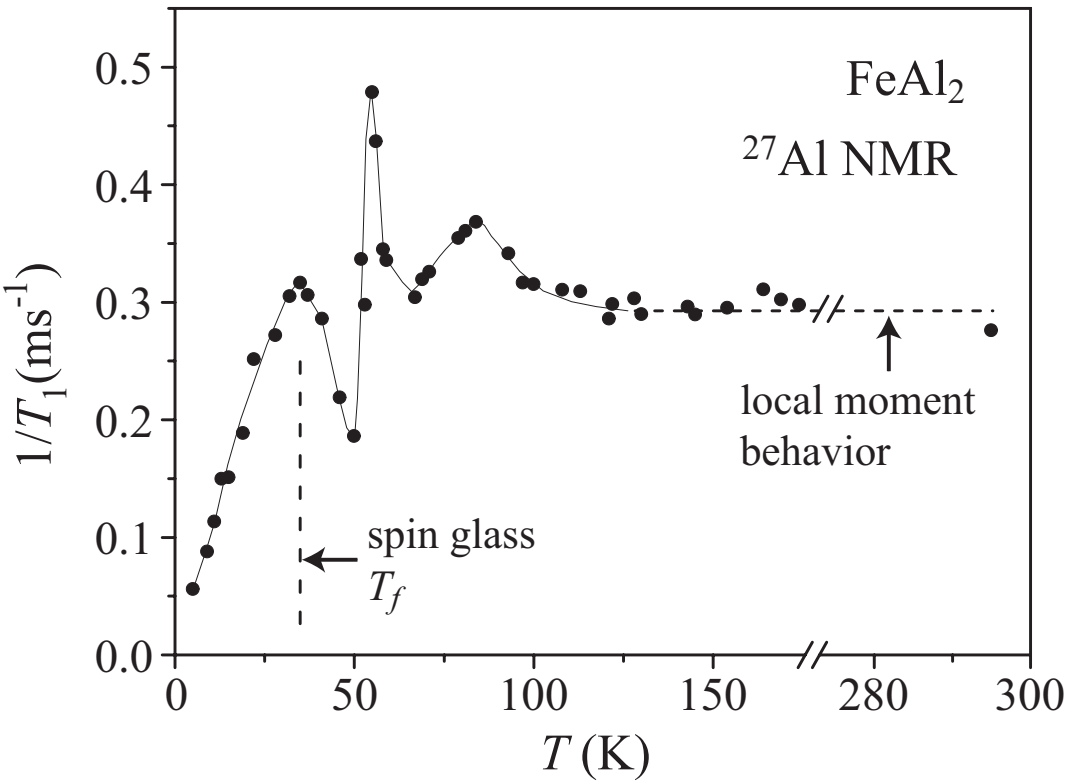

Fig. 11. ^{27}Al NMR spin-lattice relaxation rate vs. T in $FeAl_2$. Dashed horizontal line shows T-independent local-moment behavior at high temperatures. Solid curve is a guide to the eye.

moment at low T associated with the anomalous T_1 behavior. For $FeAl_2$, there is no large change in moment above T_f, as evidenced by the susceptibility [21]. However, it is possible that the alignment of adjacent spins, such as the Fe pairs or triads (Fig. 4), to form combined moments, may be responsible for these features. A gradual reduction in electron density, as shown by the changes in thermopower below 100 K [22], could contribute to such spin-alignment behavior by changing the indirect spin coupling.

The temperature independent T_1^{-1} above 100 K is characteristic of concentrated local-moment systems in which J-couplings rather than thermal fluctuations control the spin dynamics. Weak itinerant ferromagnets can exhibit similar behavior [49], however for the nearly-antiferromagnetic itinerant case, more appropriate in the present situation, $T^{1/2}$ relaxation behavior is expected. Much different behavior is also observed in Al-Fe-Cu quasicrystals, where the moments are widely separated and found on a small fraction of the sites [50]. Concentrated local moments produce a rate given by [51]

$$1/T_1 = (2\pi)^{1/2}(A/\hbar)^2(3\omega_E)^{-1}S(S+1)z'. \tag{5.3}$$

Eq. (5.3) differs from reference [51] in that A is a transfer hyperfine coupling, so we include z', the number of local moments interacting with each nucleus. In our case $z' = 3.5$ and $z = 2.5$, as described above. A is the nuclear Zeeman energy corresponding to the hyperfine field $\mu_o H_{hf}^{tr} = 0.35$ T obtained above, which is $A = -2.6\times10^{-27}$ J. Given the magnitude of p_{eff}, we assumed that $S = 1$. In the mean-field approximation [52], J is related to the Weiss temperature through $Jz = \frac{3k_B\theta}{2S(S+1)}$, giving $J = 1.6\times10^{-22}$ J. This yields $T_1^{-1} = 0.6$ ms^{-1}. The observed $T_1^{-1} = 0.3$ ms^{-1} (dashed line in Fig. 11), is in good agreement with this calculated value. Thus, the T_1^{-1} behavior provides compelling evidence that the magnetic fluctuations in this system can be attributed

to stable local moments localized on Fe atoms.

The local moment in $FeAl_2$ is surprising in light of the expected Al-Fe covalency and corresponding weakening of the moment [53, 46]. A standard picture for BCC Fe-Al alloys has been that a Fe-Fe coordination number 4 or greater is required for Fe to assume its full moment [54], thus the coordination in $FeAl_2$ would appear to oppose such behavior. The Knight shifts do indicate an apparent d contribution at the Fermi level, nevertheless from the relaxation behavior we conclude that a stable local moment, rather than an itinerant mechanism, best characterizes the observed magnetism.

B. Fe_4Al_{13}

1. Sample Preparation and Structure Analysis

Fe_4Al_{13} studied here was annealed in a vacuum-sealed quartz tube at 600° C for one week, yielding a polycrystalline ingot which was used for all measurements. The sample was characterized by powder x-ray diffraction (Bruker D8 Advance) using Cu K_α radiation. Structural refinement was carried out using the GSAS software package [38, 39]. X-ray diffraction results are shown in Fig. 12. The analysis showed no evidence for a second phase. Atomic parameters are in reasonable agreement with those reported earlier.

To confirm the sample composition. The method known as energy dispersive spectroscopy, EDS, was used to identify the elements present in the specimen and wavelength dispersive spectroscopy, WDS, was carried, counting the number of x-rays events by wavelength, giving the elemental abundance. The sample prepared for the microprobe analysis was from the same ingot used for the following NMR and other measurements. To obtained a precise result, we analyzed the compositions for

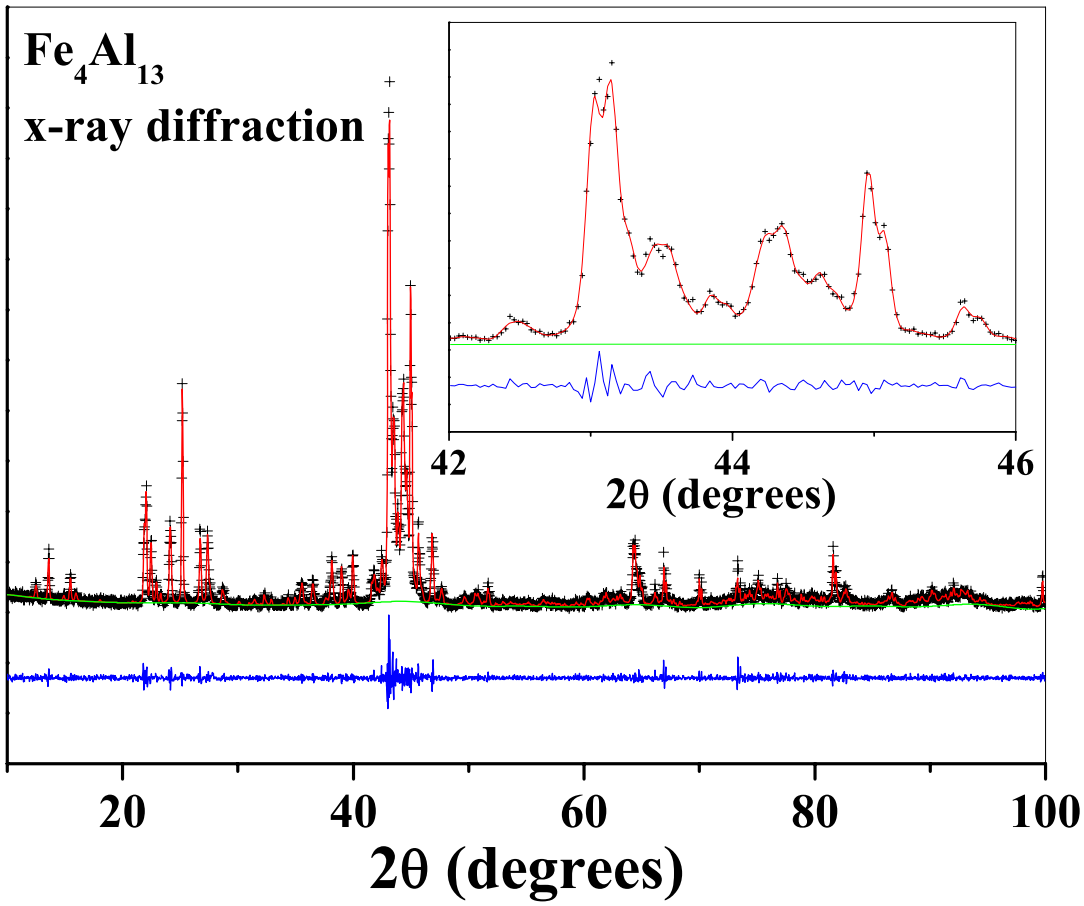

Fig. 12. Powder x-ray results for Fe_4Al_{13}, with results of refinement and difference plot.

several different sample grains and took the average for each element. The average composition for this sample is $Fe_{24.9}Al_{75.1}$.

2. NMR of Fe_4Al_{13}

We recorded ^{27}Al NMR spectra between 4 K and 454 K, using standard $\pi/2 - \tau - \pi$ spin-echo sequences. Fig. 13 displays an example of an ^{27}Al-NMR spectrum recorded at 144 K. The broad line is a superposition of powder patterns due to the 15 Al sites, giving an unresolved lineshape. From the pulse-length dependence of the spin echo, we find that the center of the spectrum represents the central (1/2$\longleftrightarrow$-1/2) nuclear Zeeman transition of Al, while the shoulders have somewhat longer 90° pulse lengths, characteristic of satellite lines [55]. For alloys, it is quite common for the quadrupole satellites to be "washed out", leaving only the central transition. Thus we treated the center of the line as a superposition of the central transitions of the various Al sites.

In Fig. 14 we show the temperature dependence of T_1^{-1} for the Fe_4Al_{13} central line between 4 and 493 K. We found that the results could be fit by assuming a parabolic pseudogap, as previously observed in a number of quasicrystals and approximants [50, 56]. The solid curve in Fig. 14 represents a fit of the form

$$T_1^{-1}(T) = aT + bT^3 + T_{1P}^{-1}, \tag{5.4}$$

with $a = 1.58 \times 10^{-3}$ K^{-1}s^{-1}, $b = 1.25 \times 10^{-8}$ K^{-3}s^{-1} and $T_{1P}^{-1} = 0.15$ s^{-1}. The small temperature-independent term, T_{1P}^{-1}, can be attributed to relaxation via dilute paramagnetic centers in combination with spin-diffusion. This term was found to be 0.17 s^{-1} in the dilute-moment system $Al_{72.4}Pd_{20.5}Mn_{7.1}$ [57], very similar to the value found here. By contrast, the corresponding term in the concentrated-moment aluminide $FeAl_2$ is three orders of magnitude larger discussed in previous section V

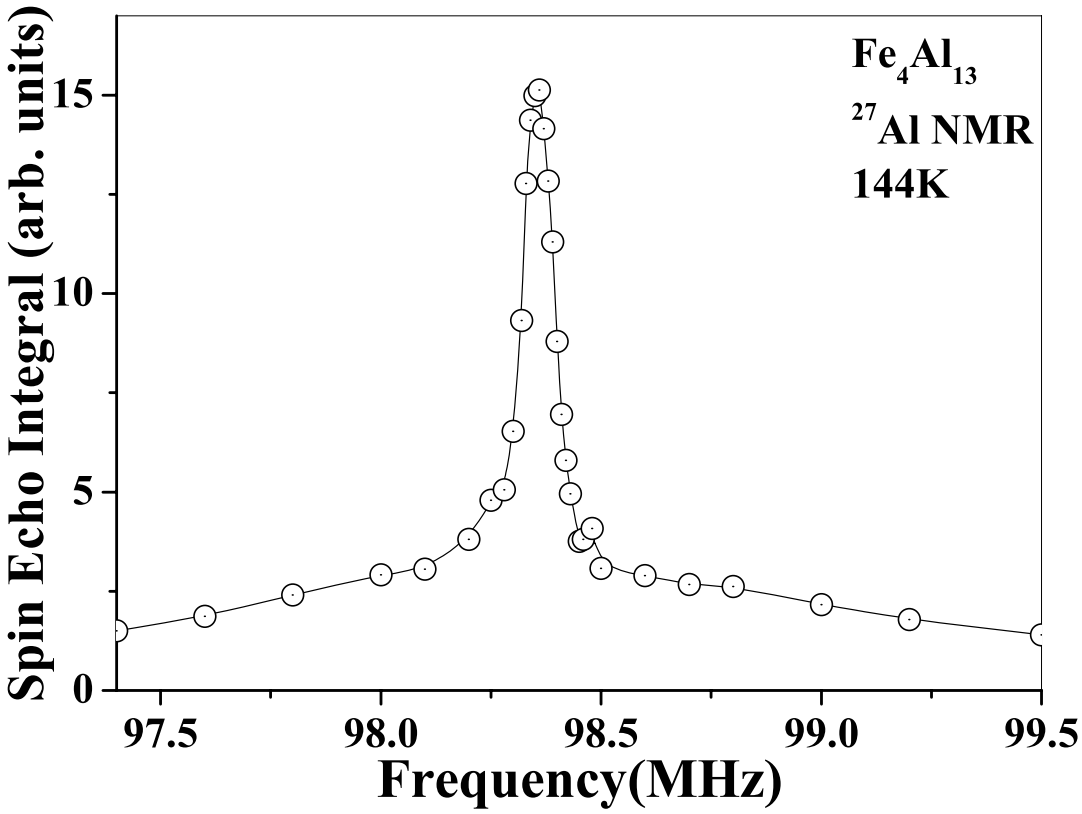

Fig. 13. 144 K ^{27}Al NMR powder pattern of Fe_4Al_{13}

(A).

T_1^{-1} due to the Fermi contact interaction between s-electrons and nuclei is given by [58]

$$1/T_{1c} = \beta_s \int dE g^2(E) f(E)[1 - f(E)], \tag{5.5}$$

according to Eq. (2.14), where $\beta_s = (64/9)\pi^3\hbar^3\gamma_e^2\gamma_n^2\langle|u_k^2(0)|\rangle_{E_F}^2$, with $\langle|u_k^2(0)|\rangle_{E_F}$ representing the squared wave function at the nucleus averaged over the Fermi surface. Since $f(E)[1 - f(E)] = -k_BT\partial f(E)/\partial E$ vanishes once E deviates from E_F by a few k_BT, the temperature dependence of $(1/T_{1c})$ is determined by the energy dependence of $g(E)$ near E_F. Assuming that the DOS in the vicinity of E_F has the form $g(E) = g_0 + \frac{1}{2}g_0''(E - E_F)^2$, Eq. (5.5) leads to

$$\frac{1}{\beta_S T_{1c}} = g_0^2 k_B T + g_0 g_0'' \frac{\pi^2}{3}(k_B T)^3. \tag{5.6}$$

This has previously been identified as the form of the Korringa relaxation for some quasicrystals [50, 56] where the DOS in the vicinity of E_F varies parabolically.

In Fe_4Al_{13}, the ^{27}Al relaxation behavior can thus be explained by the sum of the two terms described above – relaxation via conduction electrons with a pseudogap and via paramagnetic centers. The two first terms dominate the experimental data, with $a = \beta_s k_B g_0^2$, $b = \beta_s g_0 g_0''(\pi^2/3)k_B^3$. From the fitting, we obtained g_0''/g_0=325$(\text{eV})^{-2}$ and using the Al atomic hyperfine field $H_{eff,Al}^{atom} = 1.9$ MG [40], we found $g_0 = 0.011$ $\text{eV}^{-1}\text{atom}^{-1}$ (1.1 states/eV·cell), a factor 18 smaller than that of Al metal. These are similar to the values found from experiment in $Al_{62}Cu_{25.5}Fe_{12.5}$ and $Al_{72.4}Cu_{20.5}Fe_{7.1}$ icosahedral quasicrystals [50].

The average NMR shift, obtained by fitting the central portion of the line shape with a Lorentzian at each temperature, is plotted in Fig. 15. The gradual increase at high temperatures agrees well with the parameters extracted from the T_1 analysis,

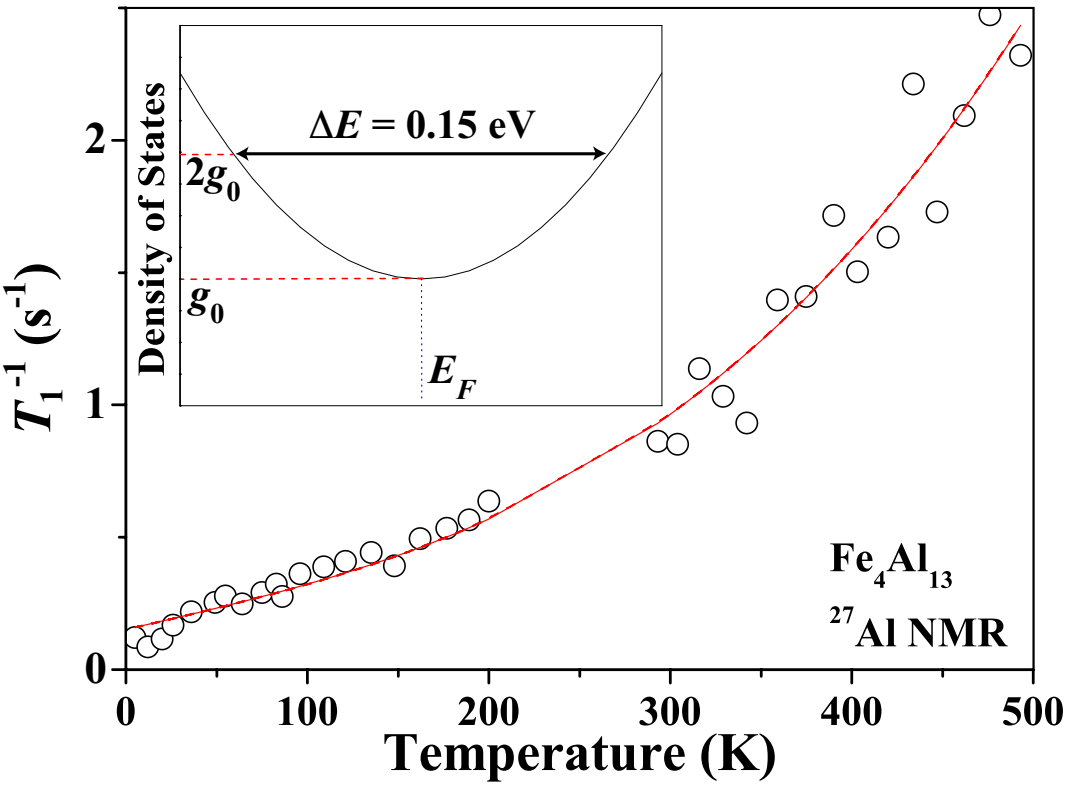

Fig. 14. Temperature dependence of relaxation rates for ^{27}Al. Solid curve: fits to the behavior described in the text. Inset: pseudogap around E_F corresponding to this fit.

with no adjustable parameters, helping to confirm that behavior. At lower temperatures the shift exhibits a magnitude change at about 75 K which is not completely understood. We have tentatively associated the drop observed below 200 K with a Curie-like tail, which is consistent with the Curie-like behavior of the linewidth (inset of Fig. 15), and also the specific-heat results described later, indicative of paramagnetic moments due to a dilute set of defects. Hence, the solid curve in Fig. 15 represents a fit of the form

$$K = K_0 + K_1(T) + K_2(T), \tag{5.7}$$

where $K_1 = C/T$ is the Curie tail, and $K_2(T)$ is obtained directly from the pseudogap parameters of Eq. (5.6). The negative K_0 = -0.077 %, obtained from the fitting, implies an Al spin polarization opposing that of the Fe d orbitals, and in aluminides such a negative line shift is found in systems with open d shells: for example this is seen in nonmagnetic FeAl [43], in the concentrated-moment system $FeAl_2$ [59] and in dilute magnetic decagonal AlPdMn quasicrystals [44]. (Note that K_0 may also contain a contribution due to the second-order quadrupole effect, since we have not removed that term.)

A negative Curie-type shift is also seen in $FeAl_2$ [59], however here the fitted Curie term is two orders of magnitude smaller, hence if this downturn in NMR shift is due to paramagnetic moments, the system of moments cannot be a concentrated one. This is similar to the result obtained from analysis of the T_1. Removing the term $K_1(T)$ from the fit, we obtain the dashed curve in Fig. 15, which goes through the lowest-temperature as well as the high-temperature data. However, the specific heat and magnetization measurements described below indicate a paramagnetic moment density that remains quite constant over this temperature range, so the source of these low-temperature changes in NMR shift remain unclear. Note that these changes are

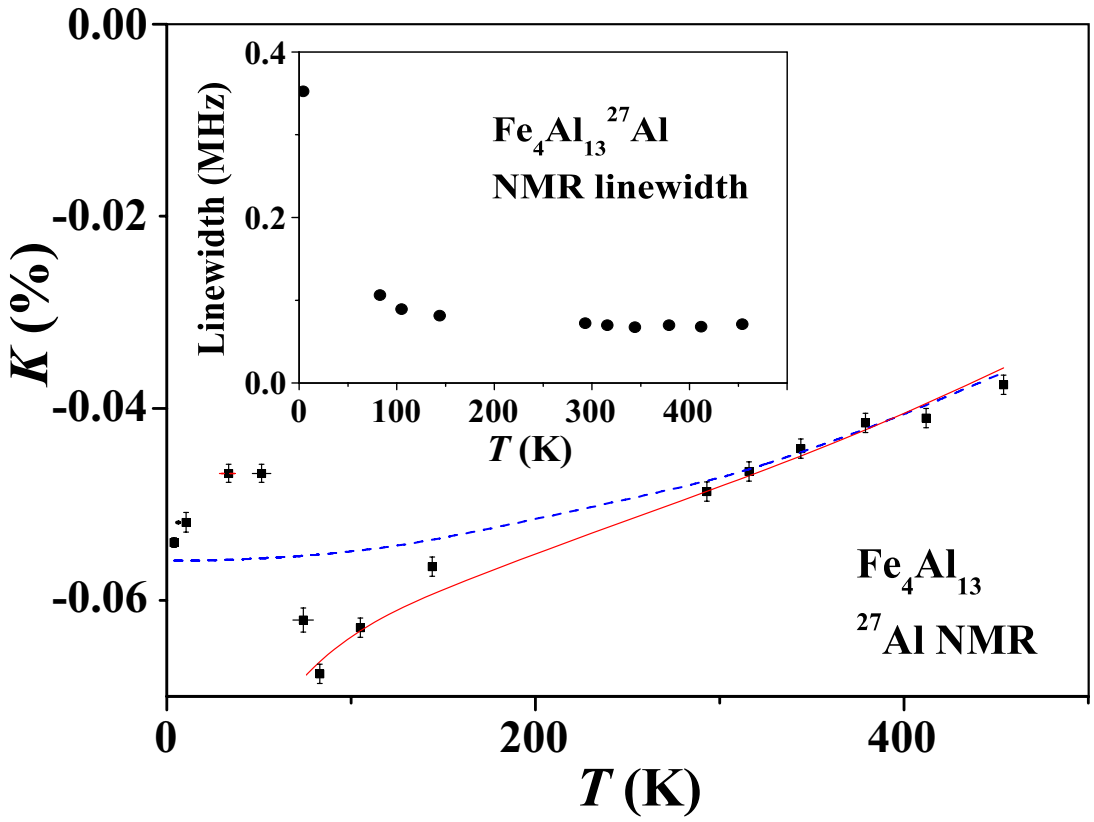

Fig. 15. ^{27}Al NMR shifts vs. temperature. Solid and dashed curves: fits described in the text, where dashed curve omits the Curie term. Inset: Temperature-dependence of ^{27}Al NMR linewidth, defined as full with at half-maximum of the NMR lineshape.

small compared to the linewidth of the low-temperature line, which is an unresolved superposition of the different Al sites. It could be that one site is more strongly affected by the paramagnetic center at low temperatures, thus wiping it out and hence changing the observed average line center. Another possibility would be a change of the conduction-electron induced super-exchange field experienced by the ^{27}Al nuclei, due perhaps to Kondo screening [60].

$K_2(T)$ is a Knight shift calculated assuming a narrow parabolic pseudogap as shown in Fig. 14. In this case the Knight shift can be expressed as [58]

$$K_2(T) = K_2^0(1 + \frac{\pi^2 k_B^2}{6}\frac{g_0''}{g_0}T^2), \tag{5.8}$$

where $K_2^0 = \frac{4}{3}\pi\hbar^2\gamma_e\langle u_k^0(0)\rangle_{E_F^0} g_0$. Using values from the T_1 fit, we calculated $K_2^0 (= 0.024\%)$ and the corresponding T^2 term, and fixed these parameters in the fit to Eq. (5.7). As can be seen, the agreement is good, showing that both the shifts and T_1 provide consistent agreement with the assumption of a parabolic pseudogap.

Existence of a pseudogap at the Fermi level in Fe_4Al_{13} has also been indicated by theoretical studies [14, 1]. The pseudogap estimated here is somewhat narrower: defining ΔE as the full width measured at points where $g(E)$ is twice the minimum value (Fig. 14), we obtain $\Delta E \approx 0.15$ eV. Similar behavior has been observed in a number of icosahedral quasicrystals and approximants, and seems to be characteristic of this class of materials [56]. Recently, similar behavior was observed in NMR studies of a decagonal quasicrystal [61], and here it has been observed in a decagonal approximant. Tunnel spectroscopy measurements of icosahedral quasicrystals also consistently show a dip in $g(E)$ centered at E_F [62, 63]. However, normally this has a characteristic square-root singularity shape, including measurements at high fields in decagonal quasicrystals [64, 65], although thermal excitations could cause rounding of the shape. Note also that tunneling probes the total DOS only [63], while ^{27}Al

NMR measures specifically the Al partial DOS, and it is possible that the narrow pseudogap in the total DOS resides only in the Al states [66].

3. Specific Heat Measurements

The 4 K linewidth of Fe_4Al_{13} (Fig. 15) is 25 times smaller than that of the concentrated-moment system $FeAl_2$ [59]. This combined with the T_1 behavior cited above shows that Fe_4Al_{13} should be regarded as a non-magnetic system containing dilute magnetic defects. To further understand the magnetic properties, the specific heat (C) was measured in the temperature range 1.8 – 300 K. A C/T vs. T^2 plot below 40 K is shown in Fig. 16 for magnetic fields 0 and 8 T. We fit the zero-field data between 23 K and 30 K to $C(T) = \gamma T + \beta T^3$, where the first term represents a standard electronic contribution and the second is due to phonons [67]. We obtained $\gamma = 5.59$ mJ/mol K^2 and $\beta = 0.408$ mJ/mol K^4, with the fit shown Fig. 16. The difference curve indicates excellent agreement over the fitted range.

Defining $C = \Delta C + \gamma T + \beta T^3$, we obtain the excess low temperature specific heat plotted in Fig. 17. The results resemble a Schottky anomaly due to magnetic defects [67] for both 0 and 8 T. We fitted the data to the multilevel Schottky function [68]:

$$C_m = Nk_B[\frac{x^2e^x}{(e^x-1)^2} - (2J+1)^2\frac{x^2e^{(2J+1)x}}{(e^{(2J+1)x}-1)^2}], \tag{5.9}$$

where N is the number of Schottky centers and $x = g\mu_B H/k_B T$, with g the effective g factor for the defect. Assuming paramagnetic spin experiencing a field of $H = 8$ T, the optimum g and J values are 1.61 and 2.21, respectively. Using these values, the effective moment per defect is $p'_{eff} = g\mu_B\sqrt{J(J+1)} = 4.3\mu_B$, and the defect concentration $c' = 0.015$ per Fe, yielding $p'_{eff}\sqrt{c'} = 0.53$. For $H = 0$, the presence of a Schottky anomaly (Fig. 17) is presumably due to an internal field acting upon the

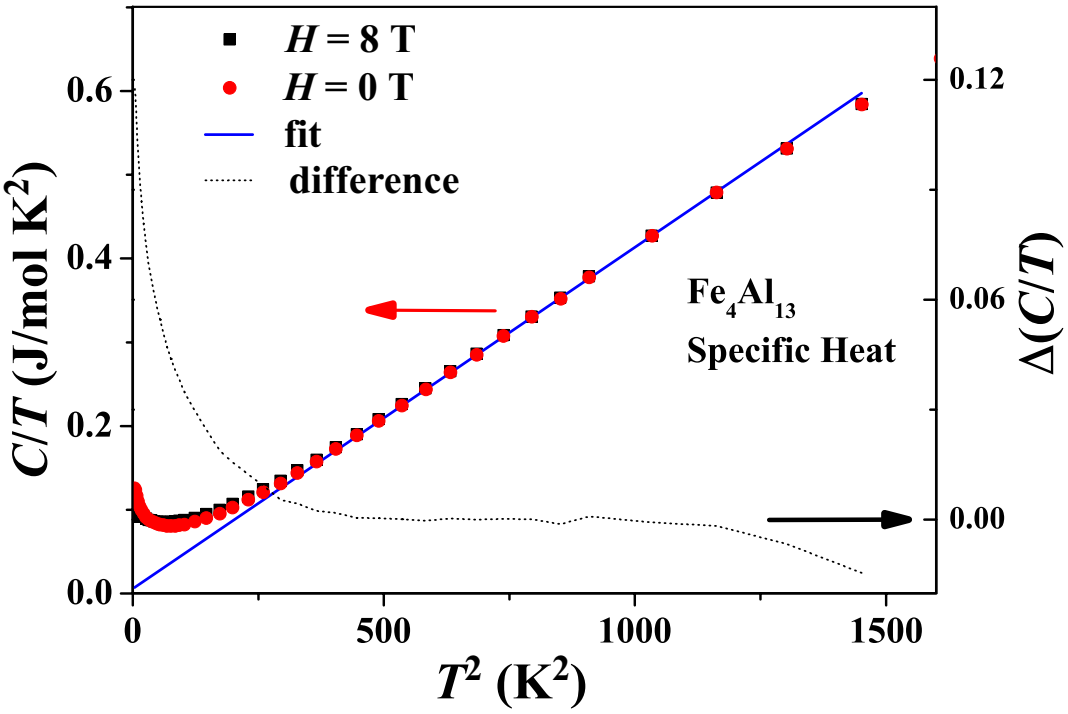

Fig. 16. C/T vs. T^2 for Fe_4Al_{13} between 0 and 40 K in fields of 0 T and 8 T. The solid curve is the fitted function described in the text and the dotted curve is the difference between the fit and the zero-field data.

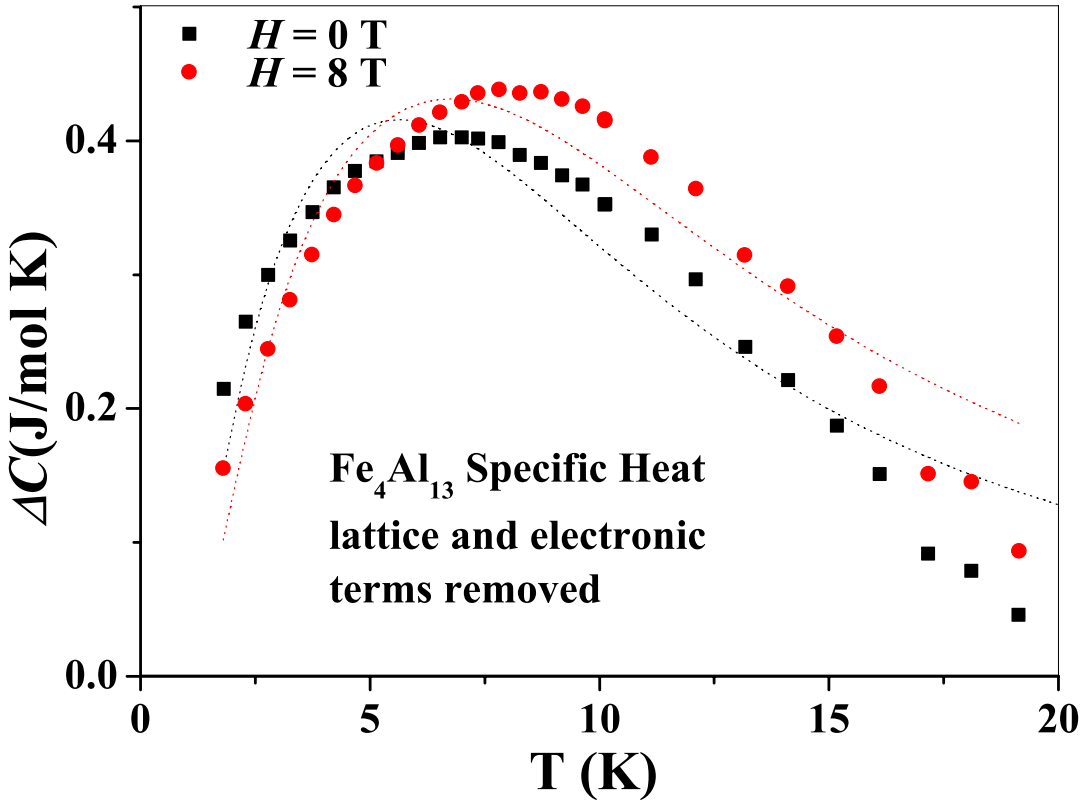

Fig. 17. Temperature dependence of ΔC in fields of 0 T and 8 T below 20 K. Curves: fits to the Schottky function described in the text

defects. Using g and J from the 8 T fit, a fit to $H = 0$ yielded an effective internal field $H_{eff} = 6.7$ T. This corresponds to a zero-field splitting which is rather typical for Fe impurities in anisotropic crystalline environments [69], although the assumed uniform H_{eff} may be a somewhat simplified model for this internal field.

A less model dependent method to estimate the moment density is provided by the magnetic entropy, plotted in Fig. 18, which is the integral of $\Delta C/T$. The total magnetic entropy thus obtained is approximately 0.8 J/mol K, including extrapolated changes below 2 K. The results are equivalent for the zero and 8 T cases, as would be expected. Using $J = 2$, the corresponding concentration of moments per Fe is

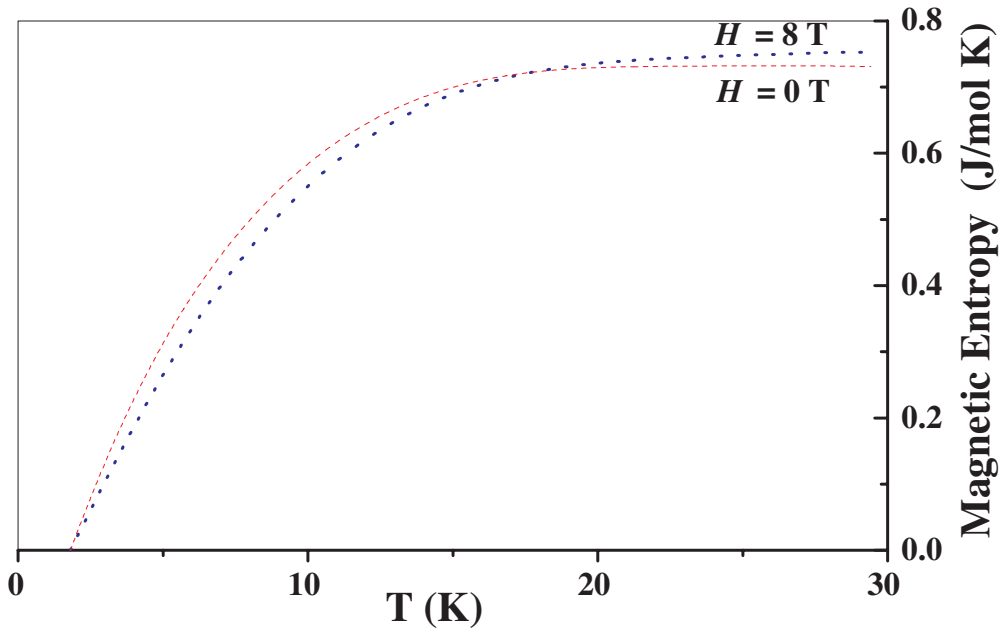

Fig. 18. Magnetic entropy extracted from specific heat in fields of 0 T (dashed curve) and 8 T (dotted curve) below 30 K.

$c = 0.2\frac{J}{molK}/N_A k_B \ln(2J+1) = 0.015$, in good agreement with the Schottky fit. This gives independent confirmation of the 4.3 μ_B moment size extracted above.

Returning to the electronic part of the specific heat, our fitted result is, $\gamma = 5.59$ mJ/mol K^2, and using $\gamma = \frac{\pi}{3} g(E_F) k_B^2$, we obtain $g(E_F) = 13$ states/(eV·unit cell). This is very close to theoretical estimates of the total $g(E_F)$ for Fe_4Al_{13} [14, 1]. In addition, $g(E_F)$ is predicted to be heavily dominated by Fe states, as confirmed here, comparing 1.1 states/eV·cell in Al-s states obtained from the small Korringa $^{27}T_1^{-1}$. Whether a parabolic pseudogap also occurs in the Fe part of $g(E_F)$ is difficult to distinguish from the specific heat; such a situation would produce a T^3 term which would be masked by the phonon term.

4. Magnetization Measurements

The dc susceptibility, $\chi(T)$, shown in Fig. 19, is of approximate Curie form but with kinks near 40 K and 200 K. Clearly the high-temperature susceptibility indicates ferromagnetic correlations. We fit the high-temperature data to a Curie law, $\chi(T) = C/(T-\theta) + \chi_d$, with

$$C = N_A c p^2 \frac{\mu_B^2}{3k_B}, \tag{5.10}$$

where N_A is Avogadro's number, c the concentration of magnetic ions per Fe, and p the effective moment. From this we obtained $\theta = 88$ K and $p\sqrt{c} = 1.05\ \mu_B$ (with c measured per Fe, fit range 200-300 K). These moments are slightly larger (per Fe) than obtained in previous measurements which fitted the curve with an additional $T^{3/2}$ term [16], and there is a clear reduction in paramagnetic moment going from these results to the moments obtained from specific heat at low temperatures. As shown below, the difference can be attributed to ferromagnetic clusters or small regions of second phase, with an ordering temperature near 200 K, which apparently dominate the high-temperature paramagnetic susceptibility. Similar magnetic clusters have been evidenced in Fe_2VAl and Fe_2VGa [21]and in quenched $FeAl_6$ [70].

The M vs. H data shown in Fig. 20 more clearly demonstrate the ferromagnetic component. In these data M exhibits a ferromagnetic saturation-type behavior at low fields, and becomes linear at higher fields. We found that the linear behavior at high fields could be modeled quite accurately according to the 4.3 μ_B paramagnetic moments, with density 0.015 per Fe, obtained from low-temperature specific heat as described above, plus an additive ferromagnetic part, assumed completely saturated at high fields. The solid curves in Fig. 20 represent such fits, with the only parameter being the additive constant at each temperature. The ferromagnetic saturation magnetization obtained as the fitting parameter is plotted in Fig. 21 vs. T. We also

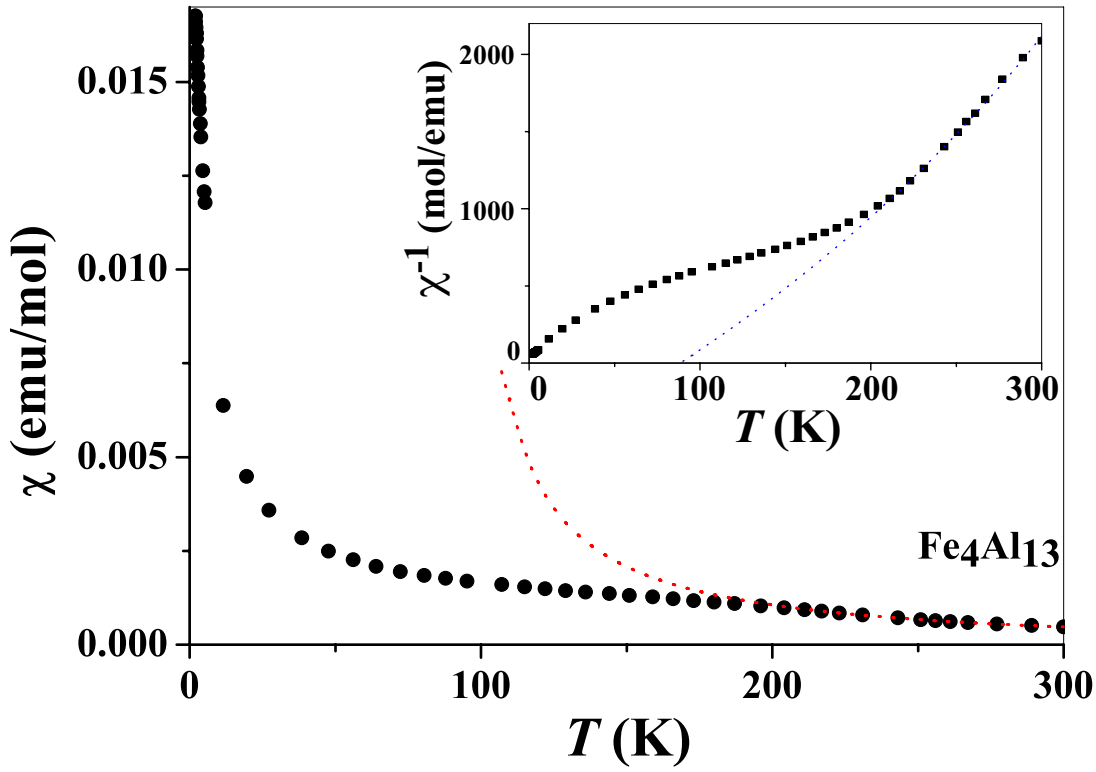

Fig. 19. The dc susceptibility $\chi(T)$, per mol Fe, in an applied field of 1000 G. Solid curve represents the Curie fit described in the text. Inset: χ^{-1} vs temperature, with curve corresponding to the the same fit.

included a mean-field saturation curve as a guide to the eye to show that the T_c for these clusters is somewhat higher than 200 K. This explains the large positive θ and the prominent kink around 200 K in the inverse susceptibility (Fig. 19), as the ferromagnetic clusters freeze below this point, and their contribution to the susceptibility is reduced.

The extrapolated $T = 0$ magnetization from Fig. 21 corresponds to approximately $3.3 \times 10^{-4} \mu_B$ per Fe, which is a small fraction of the total paramagnetic moment in the sample, as can be seen visually from the curves in Fig. 20. Since no large shifts or other features appear in the NMR data in the region below room temperature, it is clear that this ferromagnetic component is confined to clusters or small regions, and is not intrinsic to the main phase. A comparison between field-cooled and zero-field-cooled magnetization curves, measured in $H = 50$ Oe (not shown) showed very little difference over the range 4 K $-$ 300 K, indicating that this phase has a relatively low coercivity.

Since the $M - H$ curves can be modelled very well according to the paramagnetic moments obtained from low-temperature specific heat, it is clear that there is little change in the density of these moments over the temperature range up to 200 K, and there are two quite distinct moment types in the sample: a minor ferromagnetic phase plus the dilute population of 4.3 μ_B paramagnetic moments. The concentration of paramagnetic moments (0.015 per Fe corresponds to 0.36 per unit cell) is such that the moments cannot be attributed to a regular crystallographic site, since the five Fe sites each number 4/cell or 8/cell. Rather, these moments must correspond to a particular defect in the (nominally nonmagnetic) lattice. These may be formed in thermodynamic equilibrium during processing or might be associated with the partially occupied site in this structure [11, 12].

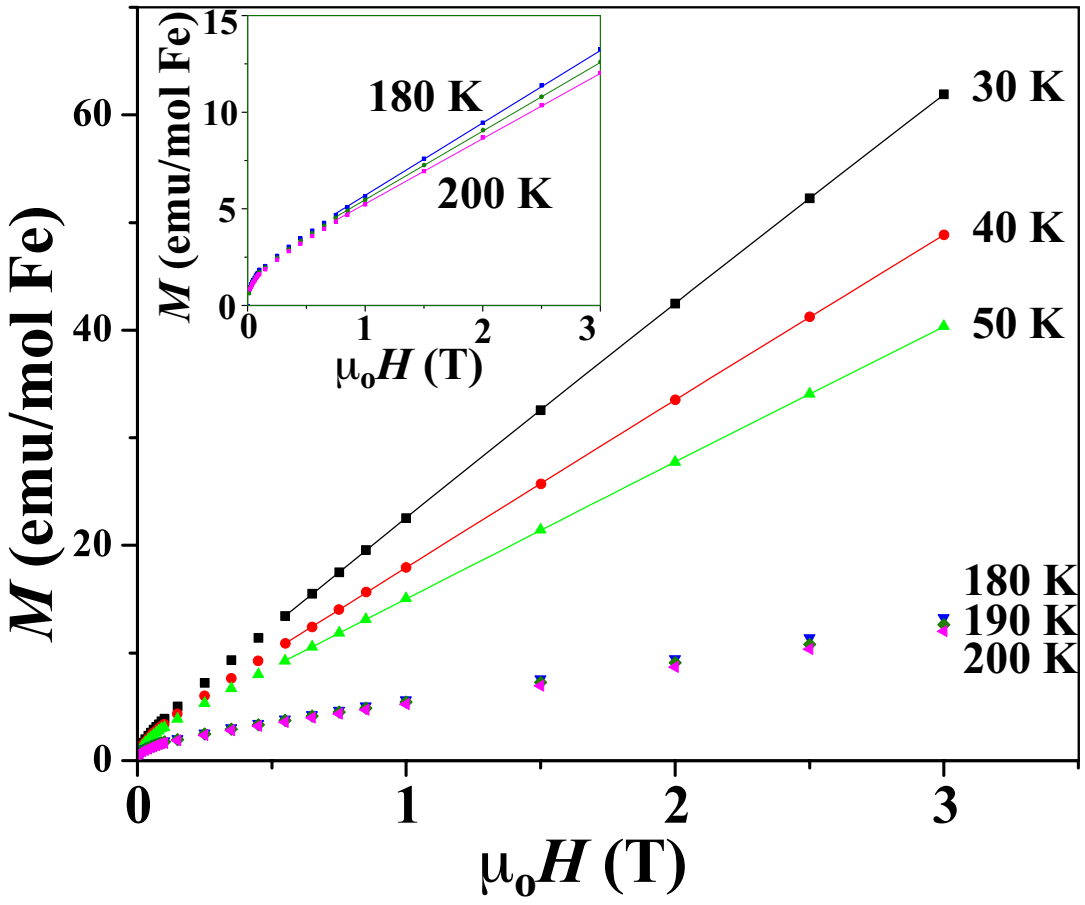

Fig. 20. Magnetization per mol Fe vs. applied field. Data from top to bottom measured at $T = 30$, 40, 50, 180, 190, 200 K. Solid curves: paramagnetic behavior identified from low-T specific heat, with a single additive constant fitting parameter. Inset: Expanded view showing data for 180, 190, 200 K, with similar theoretical curves.

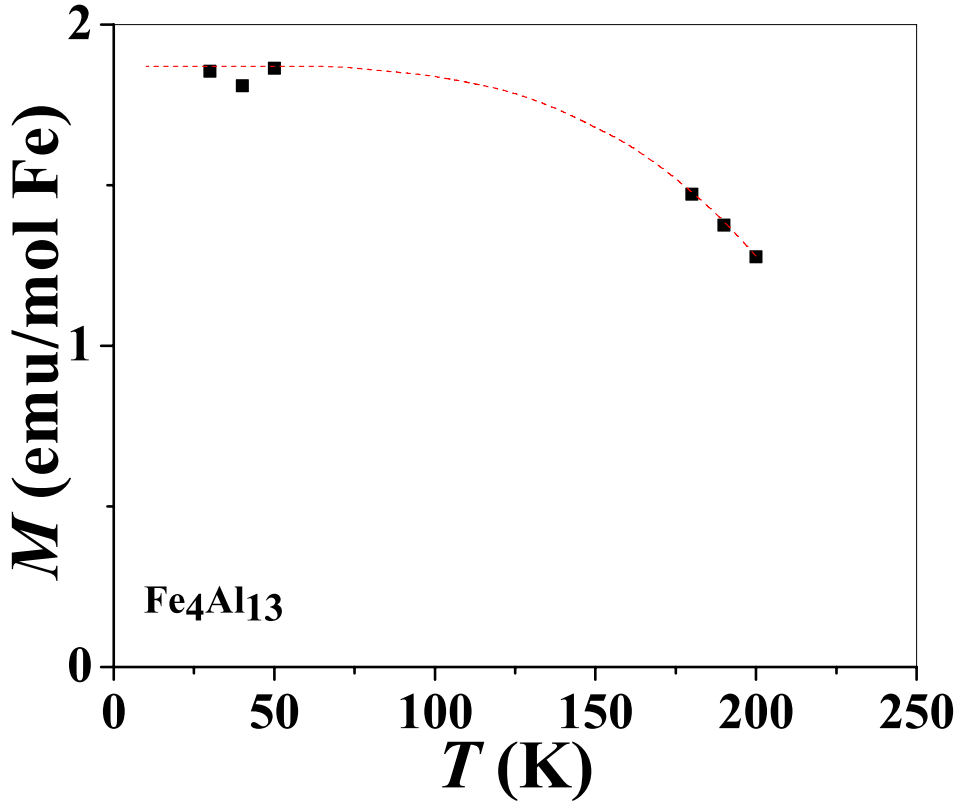

Fig. 21. Saturation magnetization for ferromagnetic clusters in Fe_4Al_{13} obtained as described in text. Curve is mean-field saturation curve, intended to guide the eye.

C. Fe_2Al_5

1. Sample Preparation and Structure Analysis

Fe_2Al_5 was also annealed in a vacuum-sealed quartz tube at 600° C for one week, yielding a polycrystalline ingot which was used for all measurements. The sample was characterized by powder x-ray diffraction (Bruker D8 Advance) using Cu K_α radiation and Wavelength Dispersive X-Ray Spectrometry (WDS). Structural refinement was carried out using the GSAS software package [38, 39].

According to the Fe-Al phase diagram, in the Fe_2Al_5 phase (Fig. 1), the molar Fe concentration could vary between 0.25 - 0.28, Fe_4Al_{12} to $Fe_4Al_{10.3}$. In the detailed structure analysis of one particular Fe_2Al_5 sample, the formula found is $Fe_4Al_{11.2}$ [19]. We prepared several samples with different starting compositions, including Fe_4Al_{10}, $Fe_4Al_{11.2}$ and $Fe_4Al_{11.8}$. WDS measurements showed 2 phases including $FeAl_2$ and Fe_2Al_5 in the samples with Fe_4Al_{10} and $Fe_4Al_{11.2}$ starting compositions. Only in a sample with starting composition $Fe_4Al_{11.8}$, no second phase was found. From WDS results, a single phase was observed with the composition $Fe_{29}Al_{71}$ ($Fe_4Al_{9.8}$) in our $Fe_4Al_{11.8}$ sample. Henceforth these samples will be reformed to according to the starting compositions, Fe_4Al_{10}, $Fe_4Al_{11.2}$ and $Fe_4Al_{11.8}$. X-ray diffraction results for $Fe_4Al_{11.8}$ are shown in Fig. 22. Atomic parameters from GSAS are in reasonable agreement with those reported earlier [19]. In our NMR measurements discussed in more details below, there is an extra peak from the highly magnetic phase $FeAl_2$ in our Fe_4Al_{10} and $Fe_4Al_{11.2}$ samples, while a single peak was found in the $Fe_4Al_{11.8}$ sample, confirming the x-ray phase analysis. The following experimental results are for the single phase $Fe_4Al_{11.8}$ sample, except as noted.

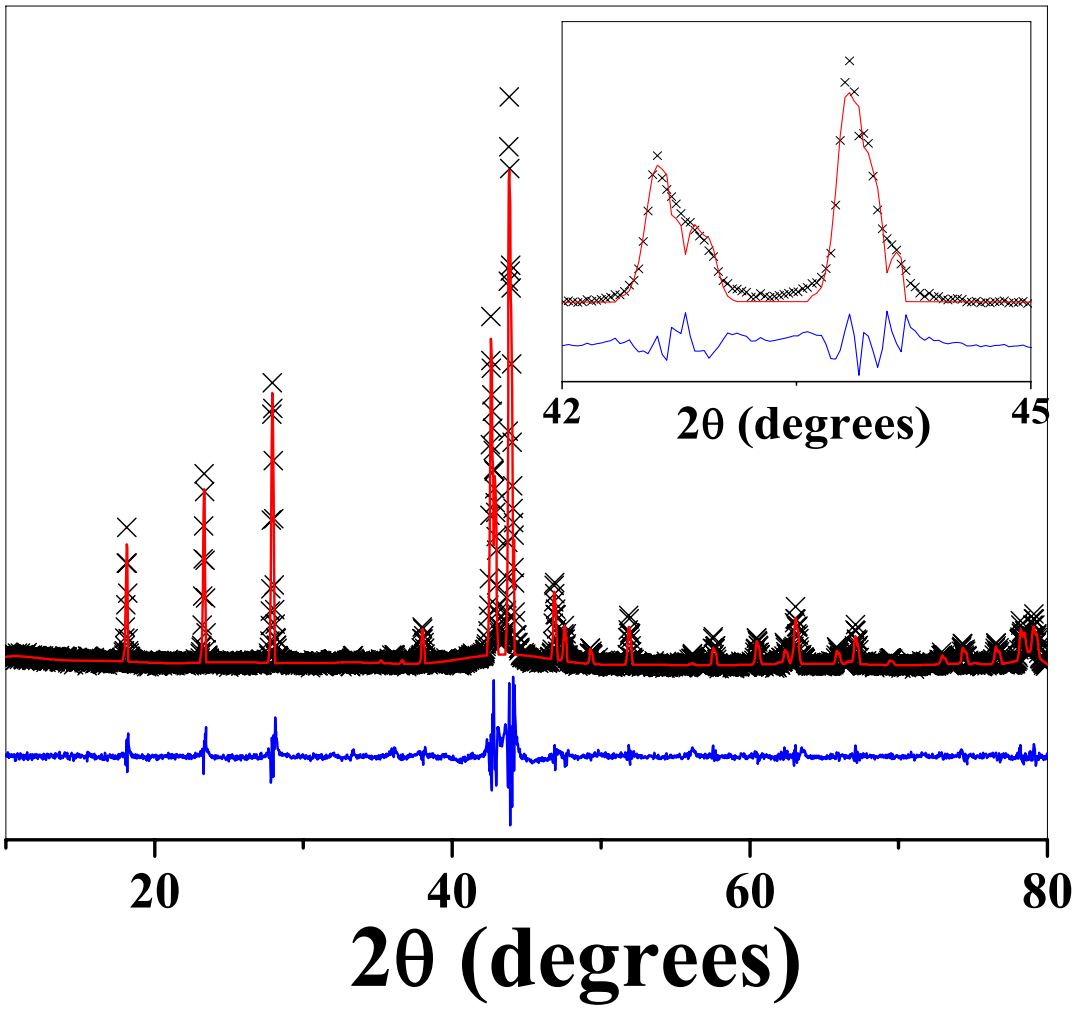

Fig. 22. Powder x-ray results for Fe_2Al_5, with results of refinement and difference plot.

2. NMR of Fe_2Al_5

In Fig. 23 we show the temperature dependence of T_1^{-1} for the Fe_2Al_5 central line between 4 and 450 K. We found that the results could be fit by assuming a narrow pseudogap, similar to what we observed in Fe_4Al_{13} [71]. The solid curve in Fig. 23 represents a fit of the form, Eq. (5.4), with $a = 3.53 \times 10^{-2}$ $K^{-1}s^{-1}$, $b = 9.43 \times 10^{-7}$ $K^{-3}s^{-1}$ and $T_{1P}^{-1} = 1.42$ s^{-1}. The small size of the temperature-independent term, T_{1P}^{-1}, confirms that Fe_2Al_5 is non-magnetic with some dilute magnetic moments, like the other dilute-moment systems, Fe_4Al_{13} [71] and typical quasicrystals [57].

Thus, in Fe_2Al_5, the ^{27}Al relaxation behavior can thus be explained by the sum of the two terms described above – relaxation via conduction electrons with a pseudogap and via paramagnetic centers. The two first terms in Eq. (5.4) dominate the experimental data, with $a = \beta_s k_B g_0^2$, $b = \beta_s g_0 g_0'' (\pi^2/3) k_B^3$. From the fitting, we obtain g_0''/g_0=109$(eV)^{-2}$ and using the Al atomic hyperfine field $H_{eff,Al}^{atom} = 1.9$ MG [40], we find $g_0 \approx 0.052$ $eV^{-1}atom^{-1}$, a factor 4 smaller than that of Al metal. Compared the value of Fe_4Al_{13} [71], Fe_2Al_5 is more metal-like with the larger $g(E_F)$.

3. Magnetization Measurements

The dc susceptibility, $\chi(T)$, shown in Fig. 24 is of approximate Curie form at high temperatures. We fit the data to a Curie-Weiss law, $\chi(T) = C/(T - \theta) + \chi_d$. From least-squares fits we obtained θ = -1.59 K and $(p\sqrt{c}) = 0.54$ μ_B. The average magnetic moment obtained this way is similar to previous measurements [16]. However, most of the studies show only a few transition metal atoms are magnetic in the rich-Al TM aluminides, which is related to the stabilization mechanism [1]. In Fe-Al system, $FeAl_2$ is a concentrated local moment system, while Fe_4Al_{13} is a dilute moment system. And the NMR results described above show Fe_2Al_5 is also a dilute moment system.

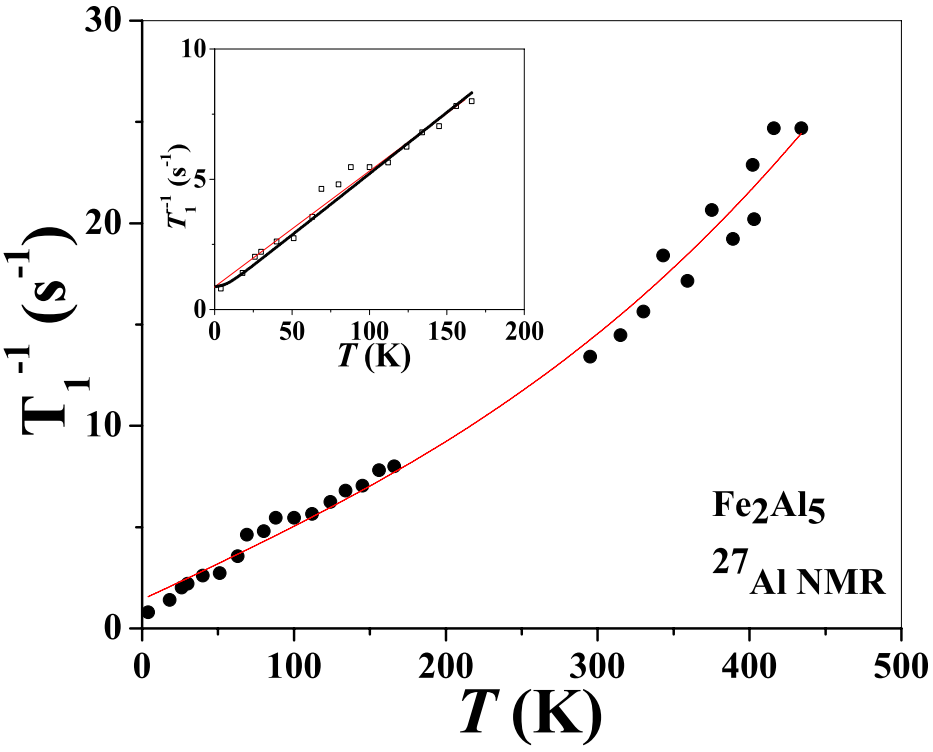

Fig. 23. Temperature dependence of relaxation rates for ^{27}Al. Solid curve: fits to the behavior described in the text. Inset: T_1 calculations. The dotted line is the calculation without the gap, the heavier solid line is the calculation with the gap, and open squares are experimental data.

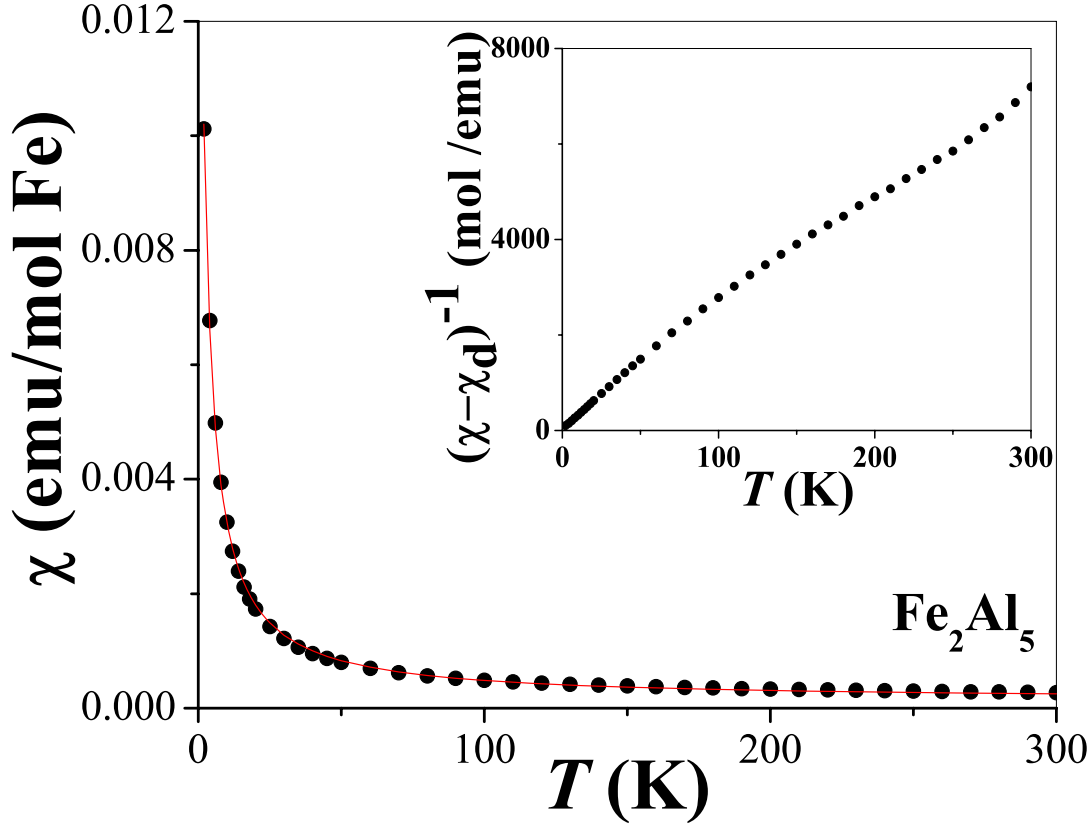

Fig. 24. The dc susceptibility $\chi(T)$ per mol of Fe in an applied field of 1000 G. The solid curve represents the Curie-Weiss fit described in the text. Inset: $\chi - \chi_d$ vs. temperature.

4. Specific Heat Measurements

To better understand the electronic structure in Fe_2Al_5, the specific heat (C) was measured in the temperature range 1.8 -300 K. A C/T vs. T^2 plot below 30 K is shown in Fig. 25. We fit the data between 23 K and 30 K to $C(T) = \gamma T + \beta T^3$, where the first term represents a standard electronic contribution and the second is due to phonons [67], and obtained $\gamma = 47.86$ mJ/mol K^2 and $\beta = 0.1469$ mJ/mol K^4, with the fit shown Fig. 25. By removing the phonon part, $\Delta C/T$ shows a minimum around 8 K and becomes constant above 20 K, as shown in Fig. 26. This unusual minimum behavior was also seen in the sample with the starting composition Fe_4Al_{10}, confirming that this is an intrinsic property of Fe_2Al_5. The observed behavior could be explained as due to the sum of a Schottky anomaly associated with dilute magnetic defects and an energy gap of approximately 20 K at the Fermi surface. Assuming such an energy gap at the Fermi energy, we calculated the electronic contribution by using the electronic specific heat function [67]:

$$C_e = \int_0^\infty (\varepsilon - \varepsilon_F) \frac{\partial f}{\partial T} g(\varepsilon) d\varepsilon, \tag{5.11}$$

where ε_F is the Fermi energy, $f(\varepsilon)$ is the Fermi-Dirac distribution function, and g(ε) is the density of states at energy ε. By using various forms of pseudogap including Lorentzian, triangle, parabolic, and square wells, the latter gave the best-appearing calculated result as shown in Fig. 26. We found the best fit by using a square well gap with a width of 2 meV and center at Fermi energy, which fits the data well above 10 K. This gap shape is plotted in Fig. 27. The DOS at the Fermi level is less than a few percent of g_0 however the value of the well minimum is not sensitively determined in our calculation. Below 10 K, the specific heat increases with decreasing temperature. This can be attributed to the very dilute magnetic defects also seen in

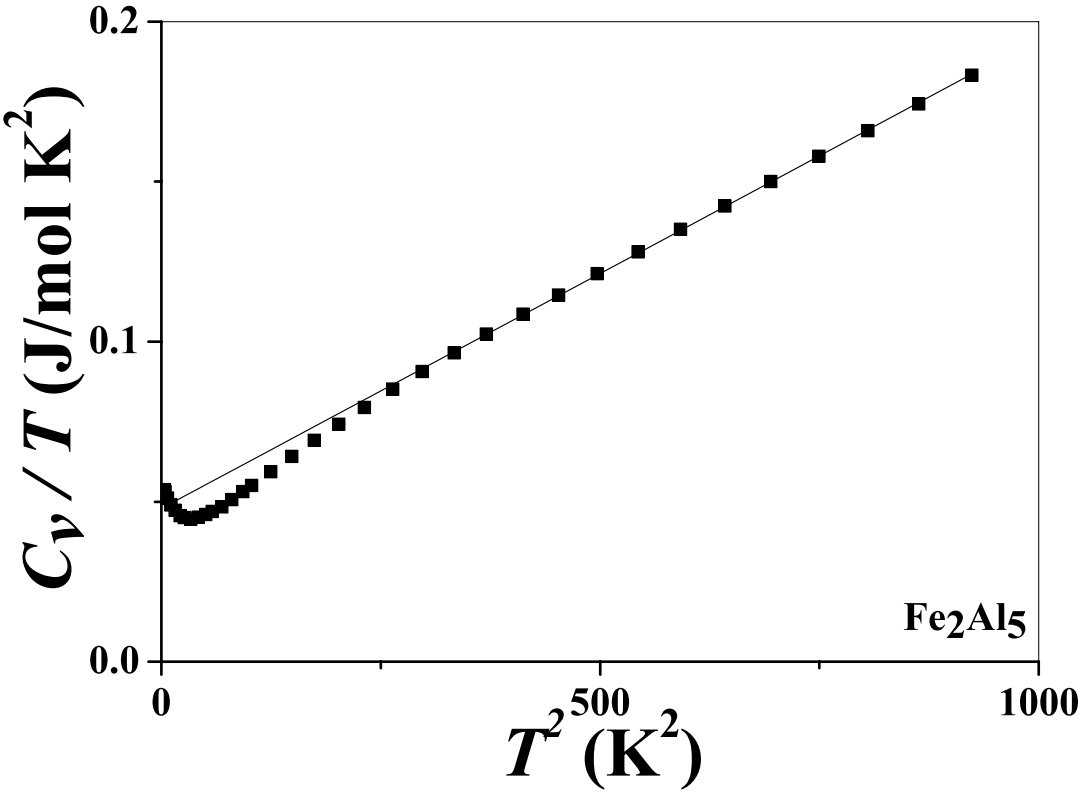

Fig. 25. C/T vs. T^2 for Fe_2Al_5 between 0 and 30 K. The solid curve is the fitted function without gap described in the text.

the T_1 measurements described above.

An alternative explanation for the low-T behavior might be an Einstein oscillation term, due to loosely-bound atoms. Indeed, some of the Fe atoms in this structure are considered in disordered channels of partially-occupied sites, making such an explanation seem reasonable. However, fits to such a model produced a broad peak in C/T above the low-T down turn [72], which did not agree with the observations. The narrow electronic gap appears to provide the best explanation for the observed data.

The broad pseudogap width estimated from ^{27}Al relaxation in Fe_2Al_5 is around 0.27 eV (Fig. 27) using the same definition of width of pseudogap in Fe_4Al_{13}. In Fe_2Al_5, we also obtained a single sharp feature of full width at half maximum 2

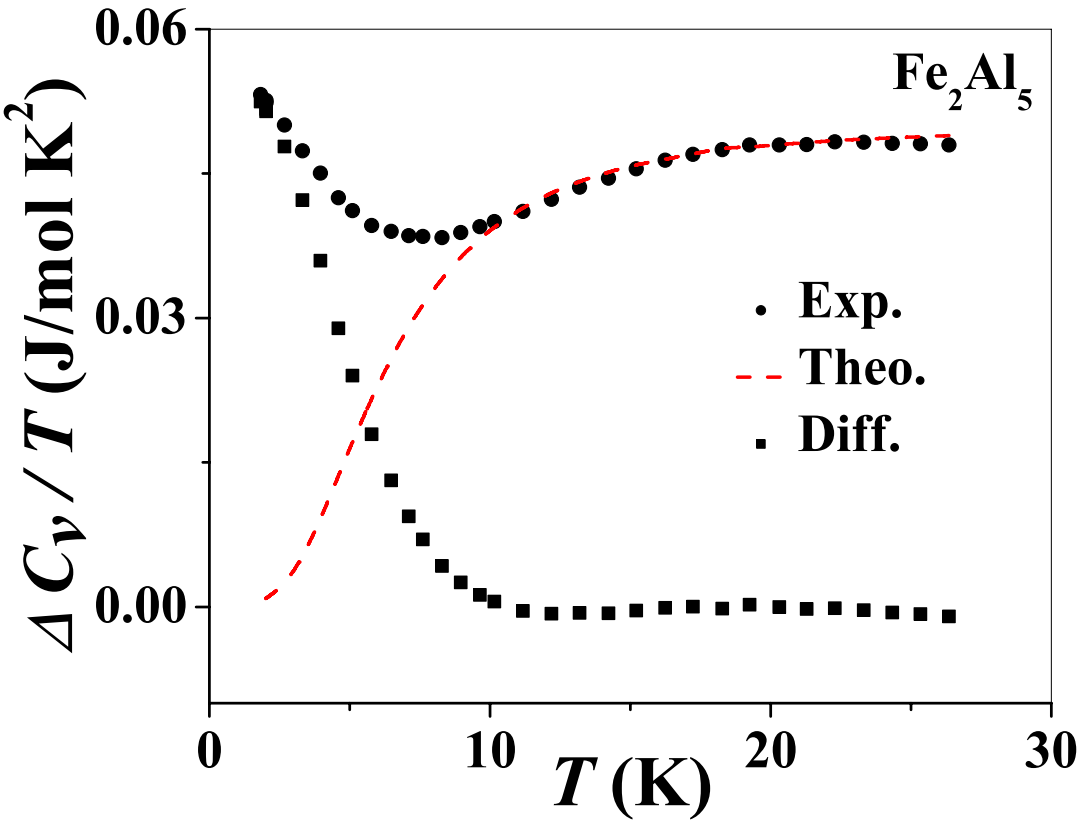

Fig. 26. $\Delta C/T$ vs. T for Fe_2Al_5 between 0 and 30 K. The solid circles are the experimental data, the open circles are the calculation results described in the text and the solid squares are the difference.

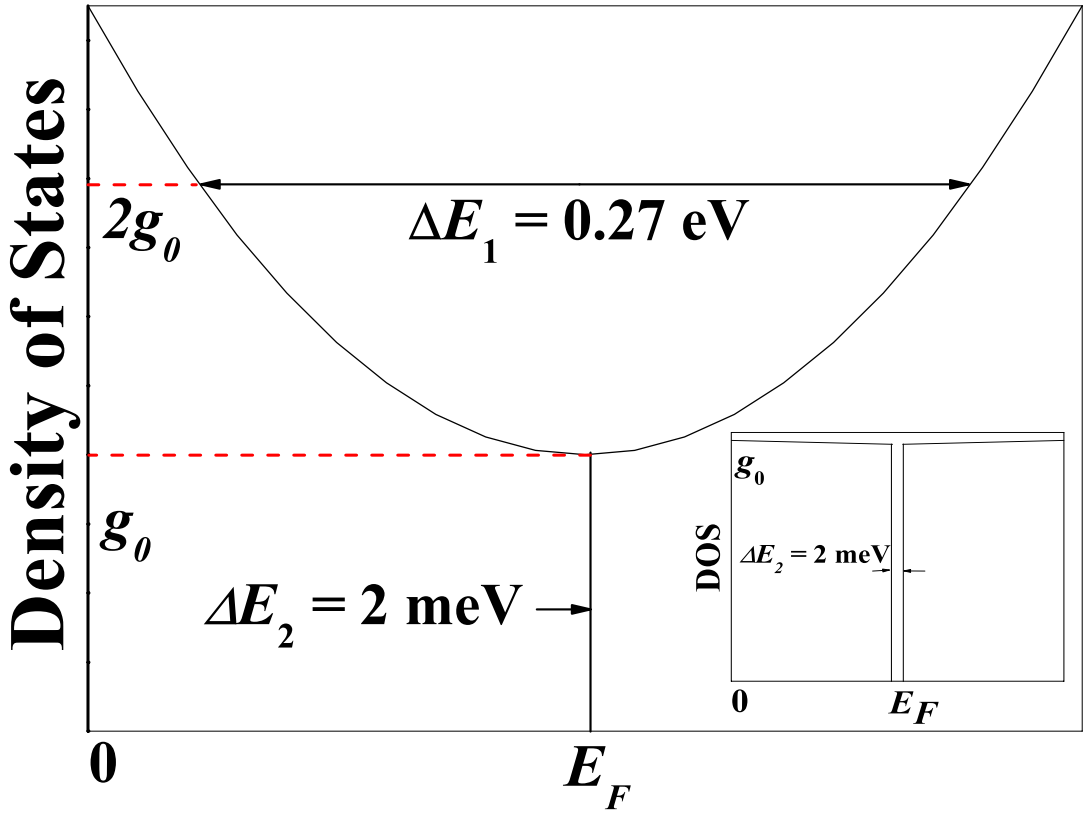

Fig. 27. Pseudogap and the single sharp feature of DOS around E_F corresponding to the fits described in the text. Inset: the narrow and deep gap at Fermi level.

meV (Fig. 27) by specific heat measurements. $Al_{70.5}Pd_{21}Re_{8.5}$ also shows a similar single sharp feature (14 meV) in NMR spin-lattice relaxation measurements [50]. We also calculated the T_1 with and without the 2 meV gap, but found no big difference between the results, shown in the inset of Fig. 23. It is due mainly to paramagnetic relaxation dominating at low temperature that we can not distinguish the difference between these two results.

Scanning tunneling spectroscopy measurements show a single square-root dip in some quasicrystals' one electron-DOS as an intrinsic property. This dip is symmetric, centered at the Fermi level, and the square root energy dependence is followed

from typically 10 meV to 300 meV [63]. This square-root dip is attributed to the electron-electron interactions in the presence of quasicrystalline structure that shares many properties with disordered systems. For disordered systems close to the metal-insulator (MI) transition, considering localization by disorder and electron-electron interaction, McMillan obtained a square-root one electron-DOS energy dependence in the metallic regime [73]. Also electron-electron interaction effects enhanced by the marginally localized character of electronic states in a quasiperiodic lattice could smooth out the spiky structured DOS predicted theoretically [74]. Even in the complex ordered structure of the approximants, this is believed to be the case. Therefore, this may explain the observed behavior in Fe_2Al_5. This single sharp feature deepens the pseudogap at E_F and represents an additional temperature-dependent reduction of the DOS that might be crucially related to the low-temperature semiconductor-like and insulator-like electronic properties of some quasicrystal families, including the metal-to-insulator transition [75]. The appearance of the sharp feature at E_F in the DOS should thus have a profound effect on the electronic DOS-related physical properties of quasicrystals and approximants.

Fe_4Al_{13} might have similar behavior, and this could be the reason for the upturn in NMR shifts at low temperatures (Fig. 15). But due to the presence of a great number of dilute magnetic defects, the possible presence of this behavior was not observed in NMR T_1 and specific heat measurements. Low-T x-ray and higher field NMR measurements might be used to further understand this behavior

D. $Al_{20}V_2Eu_x$

1. Sample Preparation and Structure Analysis

$Al_{20}V_2Eu$ sample studied here was prepared with starting composition $Al_{22}V_2Eu_{1.05}$ allowing for the evaporation of Al and Eu. The resulting ingot was annealed in a vacuum-sealed quartz tube at 650° C for two weeks, yielding a polycrystalline ingot which was used for all measurements. X-ray diffraction confirmed the anticipated $Fd\bar{3}m$ (#227) structure, while electron microprobe [wavelength dispersive spectroscopy (WDS)] indicated a $Al_{20}V_2Eu_{0.7}$ composition, with a minor Al metal second phase. Thus the Al_{16} polyhedra (Fig. 10) are filled only to 70% of the theoretical maximum in this case.

2. Magnetization Measurements

DC susceptibility results are shown in Fig. 28. High-temperature data were fit to a Curie law. We obtained $p = 5.8\ \mu_B$ per f.u. In the susceptibility results for $Al_{20}V_2La$ measured for comparison (Fig. 28), only diamagnetism was observed. Thus, the observed moment in $Al_{20}V_2Eu_{0.7}$ can be attributed to Eu. Using $c = 0.7$ (the composition obtained by WDS), 8.3 μ_B per Eu is obtained using the fit of the DC susceptibility to the Curie-Weiss law. This is slightly higher than the 7.9 μ_B Eu(2^+) free-ion moment. The difference of the moment could be due to the error of WDS composition calibration, although the slightly enhanced moment is similar to results for other EuT_2Al$_{20}$ materials [27]. The extrapolated Curie temperature, $T_c = 3.7$ K, indicates ferromagnetic interactions, and an apparent ferromagnetic transition near 4 K was observed-based on a singularity in the magnetization. Magnetization measurements extending to a lower temperature range measurement will be helpful to better understand this behavior.

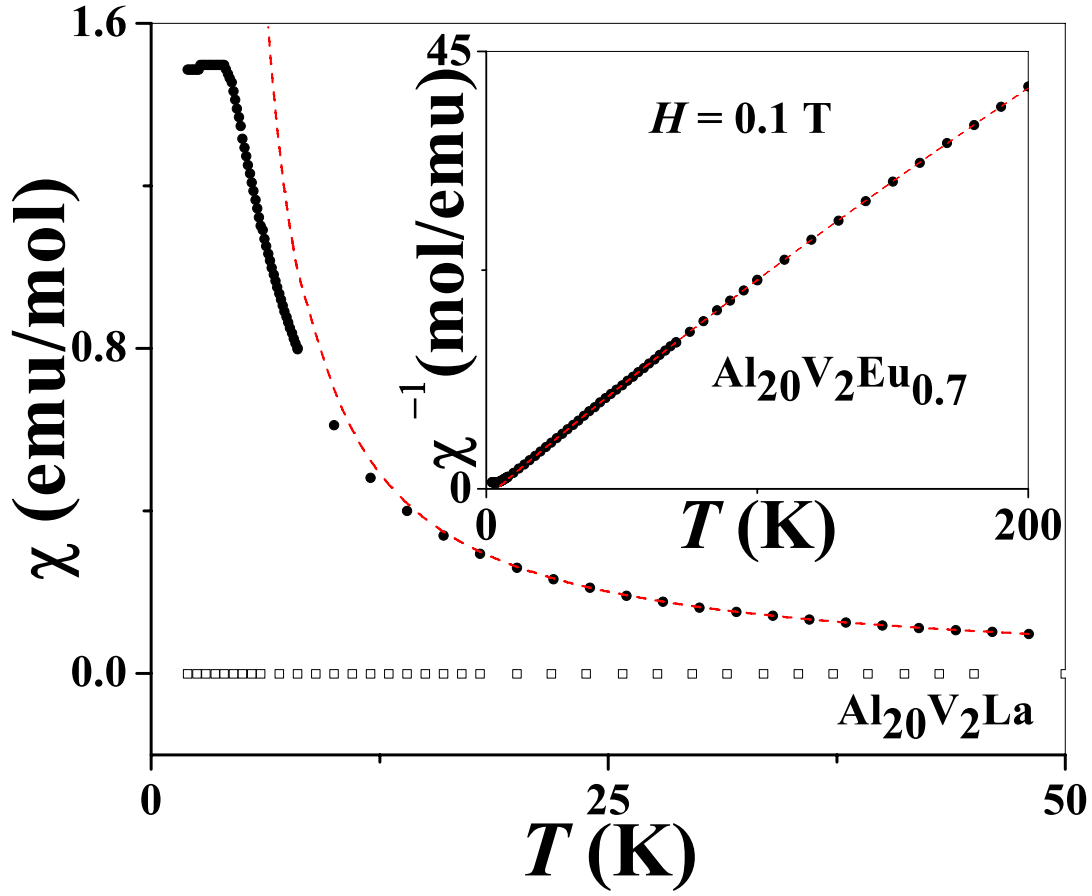

Fig. 28. The dc susceptibility $\chi(T)$, per mol $Al_{20}V_2Eu_{0.7}$, in an applied field of 100 G. Dashed curve represents the Curie fit described in the text. Open squares represent the susceptibility results of $Al_{20}V_2La$. Inset: χ^{-1} vs temperature, with curve corresponding to the the same fit.

3. Specific heat Measurements

Specific heat (C) was measured from 1.8 to 300 K in fields between 0 and 8 T. C/T is plotted vs. T^2 in Fig. 29. Below 10 K, a Schottky anomaly is observed, however between 22 and 32 K a straight-line $C/T = \gamma + \beta T^2$ fit was obtained, with electron and phonon contributions γ and β, respectively [67]. γ increases steadily from 45 to 344 mJ/(K mole f.u.) with field up to 8 T (or up to 490 mJ/K mole Eu), shown in Fig. 30. This is unlikely to result from transition orbitals and thus appears to signal participation of Eu moments in the conduction band, with a moderately heavy Fermion state at the highest field available in our apparatus. The magnetic transition was also observed around 4 K in specific heat measurements with zero magnetic field (inset of Fig. 29), consistent with the susceptibility results.

4. NMR Measurements

To further understand the properties, ^{27}Al NMR experiments were performed. We recorded ^{27}Al NMR spectra between 4 K and 415 K, using standard $\pi/2 - \tau - \pi$ spin-echo sequences. Fig. 31 displays an example of an ^{27}Al-NMR spectrum recorded at room temperature. The broad line is a superposition of powder patterns due to the 3 Al sites, giving an unresolved lineshape. From the pulse-length dependence of the spin echo, we find that the center of the spectrum represents the central (1/2$\longleftrightarrow$-1/2) nuclear Zeeman transition of Al, while the shoulders have somewhat longer 90° pulse lengths, characteristic of satellite lines [55]. Also the signal from ^{51}V overlapping with the Al satellite lines (Fig. 31) was observed. The peak of ^{51}V NMR signal moves to the lower-frequency side of ^{27}Al with decreasing temperature.

In Fig. 32 we show the temperature dependence of T_1^{-1} for the $Al_{20}V_2Eu_{0.7}$ central line between 5 and 450 K. Above 40 K metallic-like Korringa behavior ($T_1^{-1} \propto T$)

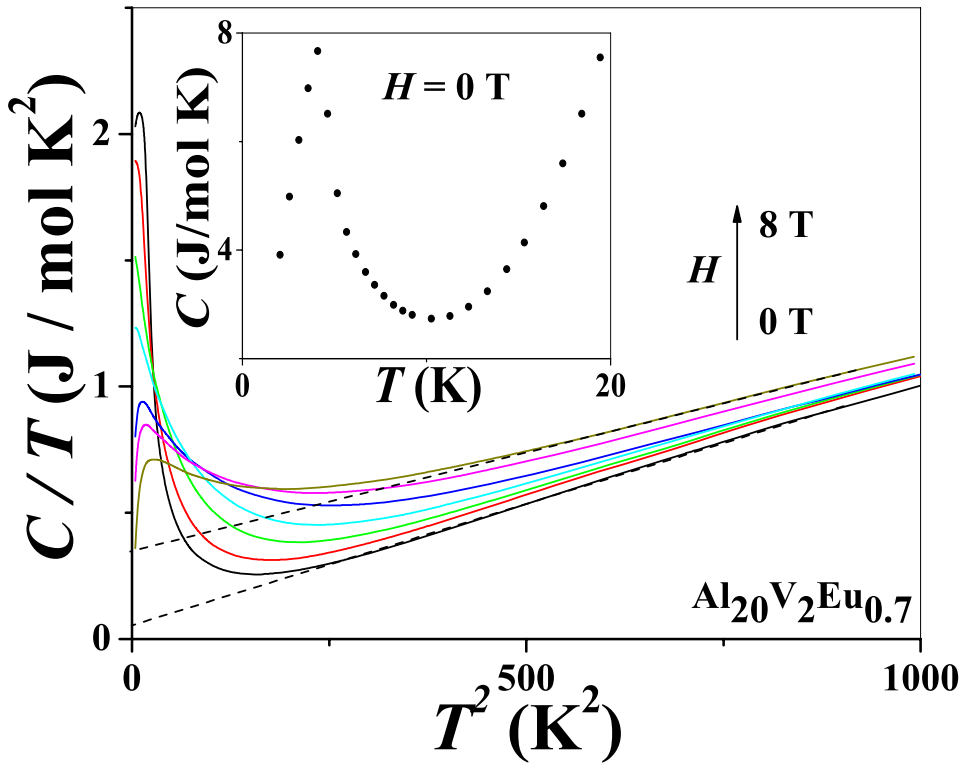

Fig. 29. C/T vs. T^2 up to $(32\ \mathrm{K})^2$ in fields between 0 T and 8 T. Dashed lines: $\gamma + \beta T^2$ fits for 0 and 8 T. Inset: Specific heat results at $H = 0$ T

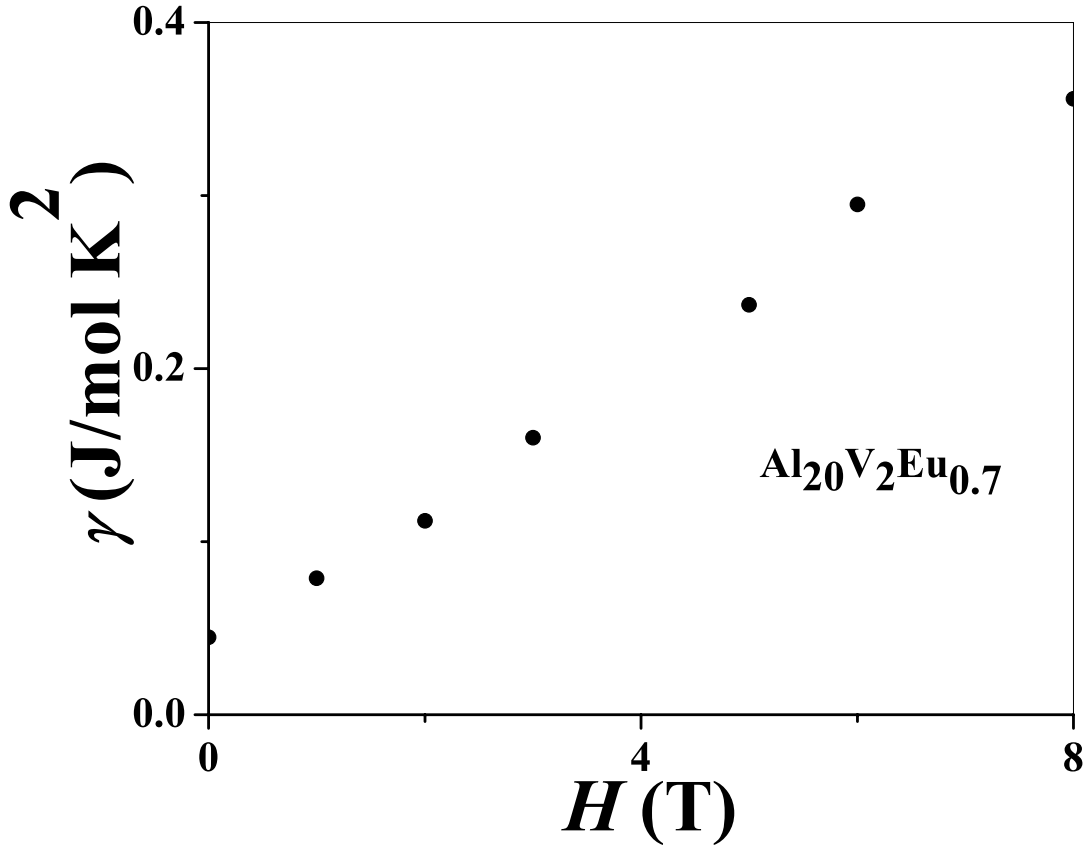

Fig. 30. γ vs. field.

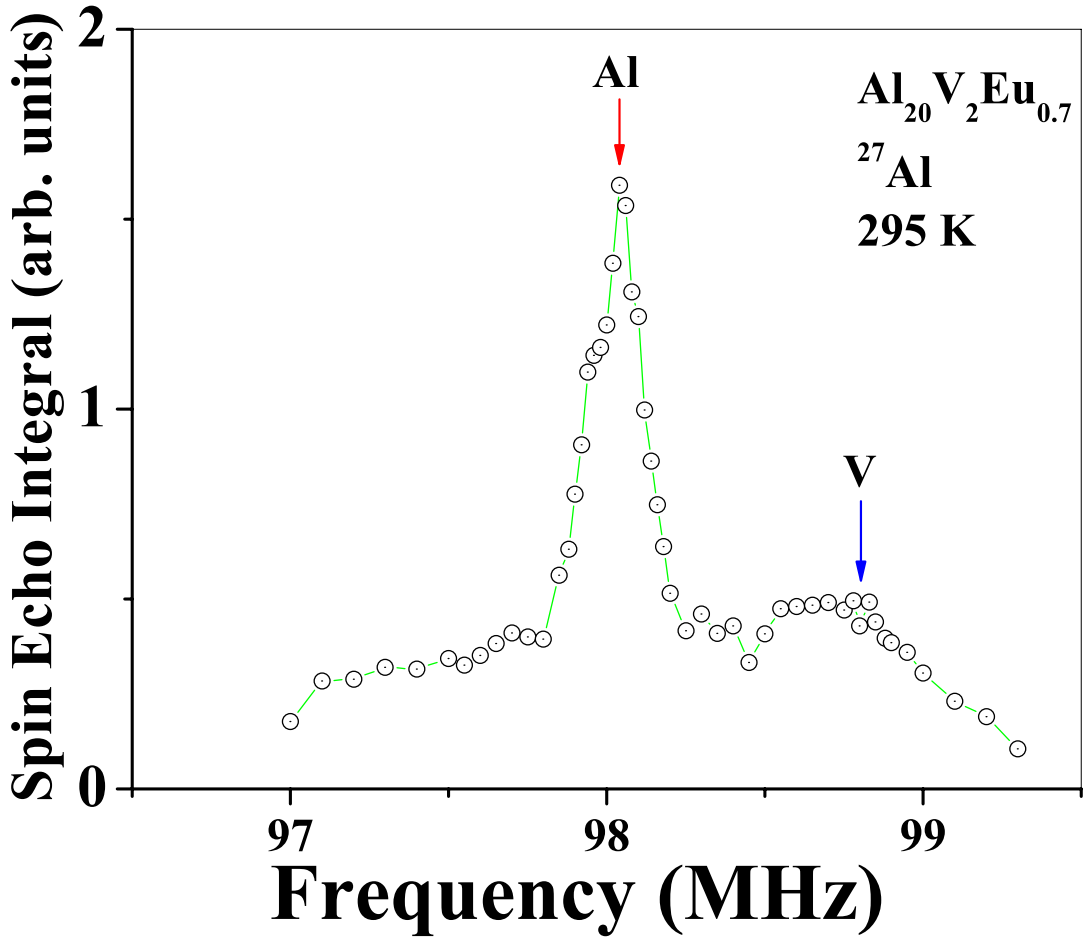

Fig. 31. 295 K ^{27}Al NMR powder pattern of $Al_{20}V_2Eu_{0.7}$

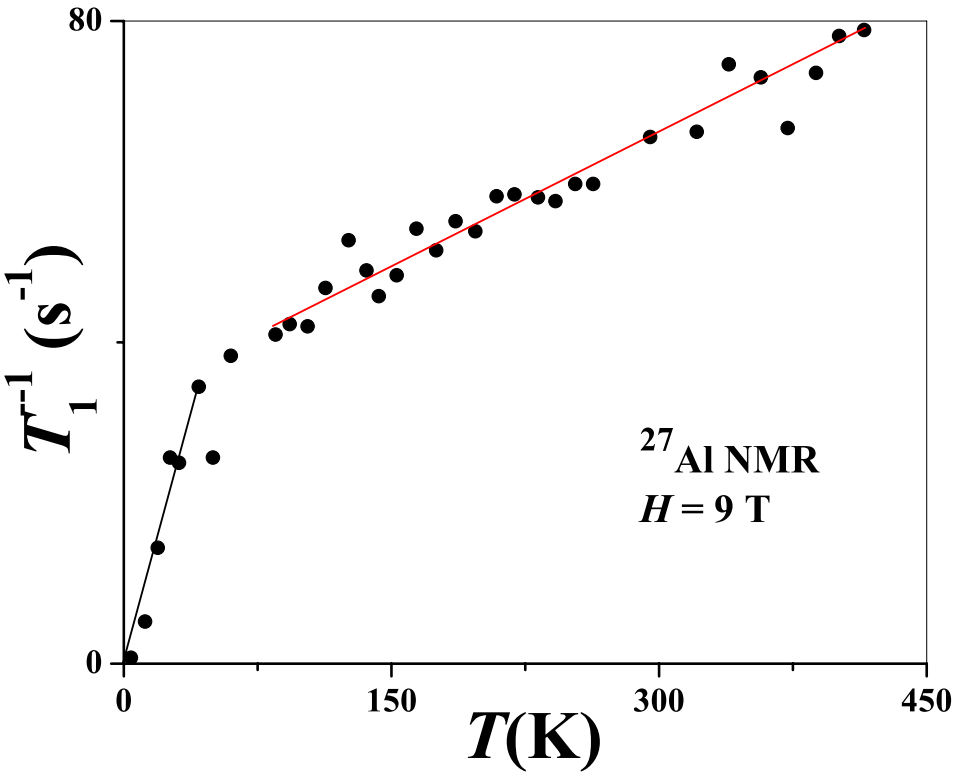

Fig. 32. Temperature dependence of relaxation rates for ^{27}Al. Solid curve: fits to the behavior described in the text.

is observed plus a large temperature-independent term due to rapidly fluctuating local moments. Such behavior is typical of concentrated paramagnetic metals[59]. Near 40 K, $T_1^{-1}(T)$ exhibits a clear change, with a larger Korringa slope and little local moment behavior. The increasing of the Korringa relaxation slope confirms the hybridization-enhanced density of states at the Fermi level from specific heat results. The disappearance of the local-moment term is consistent with the enhanced γ, and similar behavior is seen in dense Kondo systems such as $CeNiAl_4$ [76].

The average NMR shift and linewidth (the full width at half-maximum of the

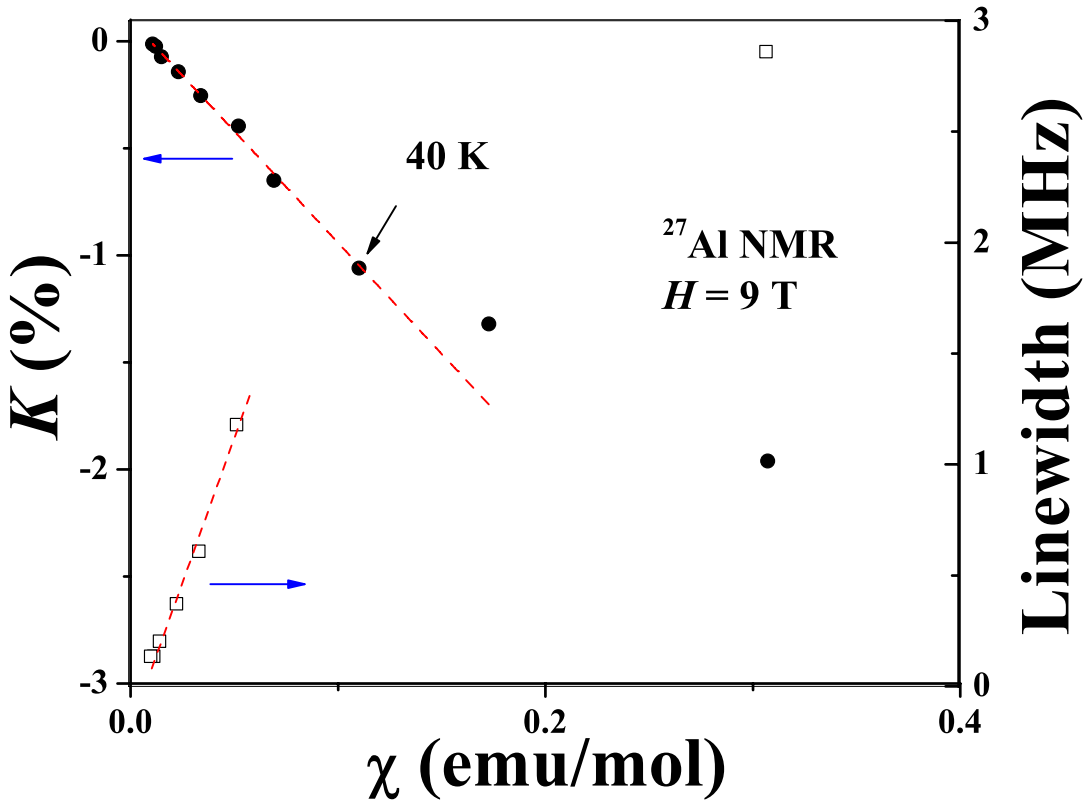

Fig. 33. ^{27}Al NMR shifts and FWHM linewidths vs. χ for $Al_{20}V_2Eu_{0.7}$.

NMR line) were measured at each temperature, and plotted against the magnetic susceptibility in Fig. 33. At high temperature, the NMR shift and linewidth are proportional to the susceptibility, corresponding to ^{27}Al directly coupled to neighboring Eu moments, with a negative transfer hyperfine coupling. Similar behavior was also observed in other paramagnetic systems [59]. Below 40 K, a deviation observed in the NMR shift and linewidth vs. χ reflects a change-over to a new magnetic regime, which is consistent with the T_1 behavior. This breakdown in the dependence on χ has been observed in various Kondo systems [77].

$M - H$ measurements at high magnetic fields also show a similar moment loss, as shown in Fig. 34. In this figure, we used Brillioun functions for $M(H, T)$ based on

the paramagnetic moment obtained from high-T Curie fits to calculate the theoretical values. The upturn with decreasing temperature is due to the absence of θ in the Brillouin function, however a divergence between different curves is seen near 40 K, the same as the NMR crossover temperature.

Fig. 35 shows the resistivity results at different magnetic fields. Without magnetic field, a Kondo-type behavior, in other words a resistivity upturn with decreasing temperature, is observed. By applying the field, the Kondo behavior is drastically suppressed consistent with the loss of the magnetic moment in susceptibility and NMR measurements, and a non-Fermi-liquid-like behavior, $\rho \propto T^D$ $(1 < D < 2)$, is found below 40 K, characterized by an enhanced electronic density of state at E_F. Non-Fermi-liquid behavior is often observed at a position in the phase diagram near a magnetically ordered state, indicating that non-Fermi-liquid behavior may be related to magnetic instability that arises at $T = 0$. The transition from magnetic order to a non-Fermi-liquid state is driven by a control parameter other than temperature, e.g., external pressure, composition or magnetic field at $T = 0$. The control parameter thus tunes a system at $T = 0$ from an ordered ground state towards a non-ordered state crossing a quantum critical point [78, 79]. The non-Fermi-liquid-like behavior between Kondo low field and Fermi-liquid high field regimes in $Al_{20}V_2Eu$ could be a consequence of a field driven crossover from a magnetic to a non-magnetic state. However, the apparent linear-T^2 resistivity can only be observed over a rather small temperature range. Ultra-low temperature and higher magnetic field measurements would be useful to confirm the non-Fermi-liquid-like to Fermi-liquid transition.

Field-induced heavy Fermion behavior has been observed in $Ce_{0.5}La_{0.5}B_6$ [80] and $PrFe_4P_{12}$ [81], however these cases are associated with antiferroquadrupolar interactions. It may be that the present enhancement is attributable to a field effect on the narrow electronic density of states features of the $Al_{10}V$ framework [24]. This may

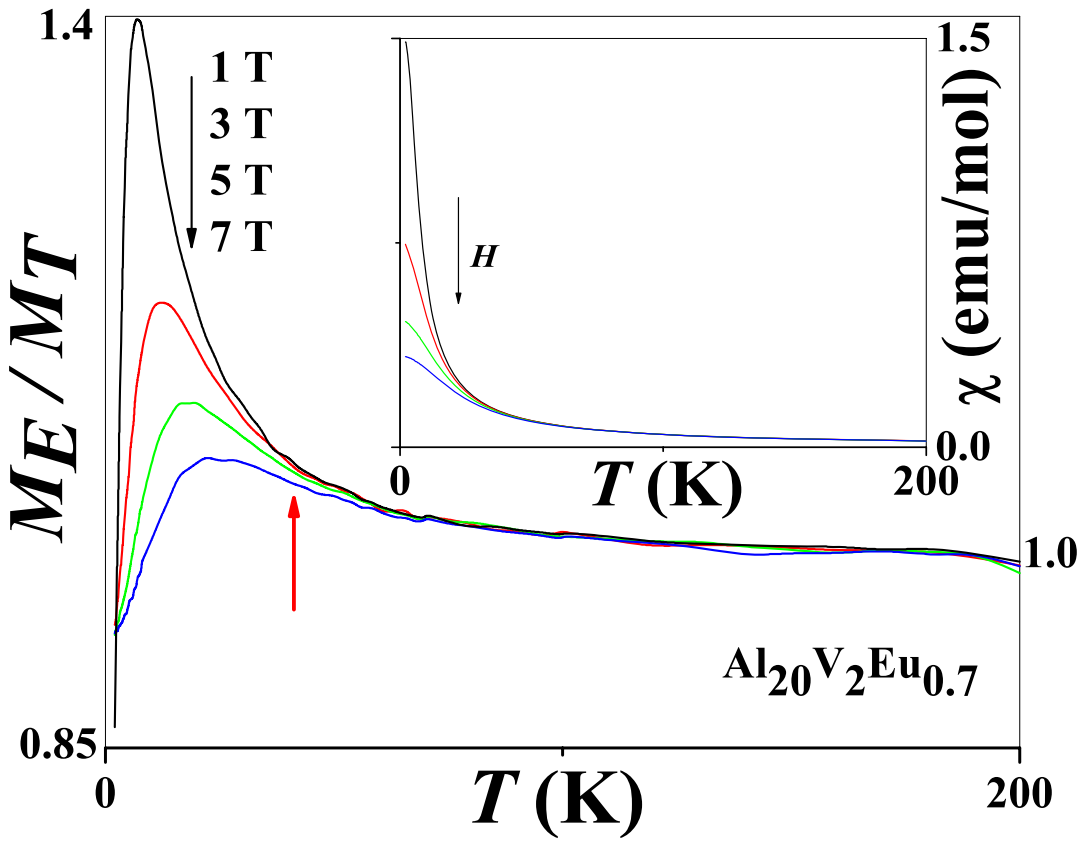

Fig. 34. Experimental/theoretical magnetization ratios, described in text, for the indicated fields. Inset: DC susceptibility result at high magnetic fields.

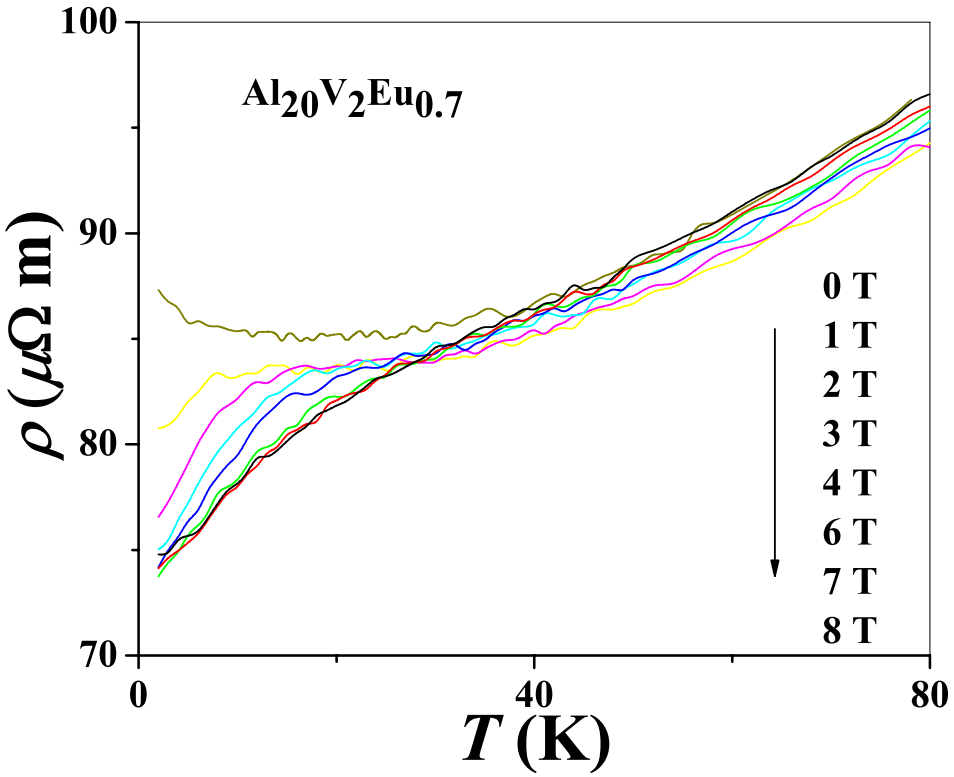

Fig. 35. Resistivity vs. temperature at different magnetic fields.

be akin to the behavior of SmB_6 [32], a Kondo insulator, in which the Kondo gap can be closed and the electron mass increased by the presence of an applied magnetic field. Theoretical studies show that the magnetic field changes the sign of the magnetization of conduction electrons, thus the Kondo effect dominates by aligning the spins of conduction and f electrons in opposite directions, and thus Kondo correlations produce the large mass enhancement [34]. Experiments at higher magnetic fields may help to further elucidate the changes in $Al_{20}V_2Eu$, since apparently the mass enhancement has not saturated even at 8 T.

CHAPTER VI

CONCLUSION

In summary, the magnetism in Al-rich Fe-Al systems is quite varied. Both Fe_4Al_{13} and Fe_2Al_5 are non-magnetic, typical behavior for transition-metal aluminides. NMR measurements show dilute paramagnetic moment behavior. Specific heat results demonstrate the presence of 4.3 μ_B dilute magnetic impurities in Fe_4Al_{13}. However, $FeAl_2$ is characterized as a concentrated local moment system by NMR T_1 measurements, and spin-glass transition at low temperature is confirmed.

I have shown measurements of several related transition metal aluminide systems. Results for Fe_4Al_{13} and Fe_2Al_5 show pseudogap behavior typical of QCs and approximants. The NMR data yield a broad energy gap of 0.15 eV and 0.27 eV but with a residual Fermi-level DOS of about $0.011 \text{eV}^{-1}\text{atom}^{-1}$ and $0.052\ \text{eV}^{-1}\text{atom}^{-1}$, in Fe_4Al_{13} and Fe_2Al_5 respectively. Thus, Fe_2Al_5 is more metal-like, however the two are rather similar in the respect.

However, besides the broad pseudogap, a deep, narrow gap of approximate width 2 meV was detected in Fe_2Al_5 by specific heat measurements. This single sharp feature might be attributed to electron-electron interactions in the presence of disorder. The upturn in the NMR shifts at low temperature of Fe_4Al_{13} (Fig. 15) could also be due to a similar sharp feature at Fermi level, however the result is less clear in that case. The appearance of the sharp feature at E_F in the DOS may thus have a profound effect on the electronic DOS-related physical properties of QCs and approximants.

$Al_{20}V_2Eu$ was studied using different methods. Magnetization results indicate a nearly 2^+ Eu valence state, and a magnetic transition near 4 K. A magnetic-field-induced heavy-fermion state was detected with a gradual enhancement of the electronic term γ by specific heat measurements. The appearance of this low-temperature

magnetic state is built from moments affected by Kondo screening, which is enhanced by application of a magnetic field. The high-field ^{27}Al NMR T_1 exhibits a crossover from local-moment behavior to Korringa-like behavior near 40 K, showing a typical dense Kondo system. Susceptibility and resistivity measurement at different magnetic fields also confirm the loss of the magnetic moment within the magnetic field. Thus these data provide a consistent picture indicating that $Al_{20}V_2Eu$ is a rare example of a Eu-containing heavy-Fermion material, with a transition into the Fermi-liquid state induced by an applied magnetic field. Experiments at higher magnetic fields may help to further elucidate the unusual changes in $Al_{20}V_2Eu$.

REFERENCES

[1] G. T. de Laissardière, D. Nguyen-Manh and D. Mayou, "Electronic structure of complex Hume-Rothery phases and quasicrystals in transition metal aluminides," *Prog. Mater. Sci*, vol. 50, pp. 679 - 788, 2005.

[2] C. Janot and R. Mosseri, *Quasicrystals*, vol. 1. World Scientific, Singapore: State of Publication, 16th edition, 1995.

[3] S. J. Poon, "Electronic-properties of quasi-crystals - an experimental review," *Adv. Phys.*, vol. 41, pp. 303 - 363, 1992.

[4] G. T. de Laissardière, D. Mayou and D. Nguyen-Manh, "Electronic-structure of transition atoms in quasi-crystals and Hume-Rothery alloys," *Europhys. Lett.*, vol. 21, pp. 25 - 30, 1993.

[5] G. T. de Laissardière, D. N. Mahn, L. Magaud, J. P. Julien, F. Cyrotlackmann and D. Mayou, "Electronic-structure and hybridization effects in Hume-Rothery alloys containing transition-elements," *Phys. Rev. B*, vol. 52, pp. 7920 - 7933, 1995.

[6] G. T. de Laissardière, E. Dankhazi, E. Belin, A. Sadoc, N. M. Duc, D. Mayou, M. A. Keegan and D. A. Papaconstantopoulos, "Experimental and theoretical electronic distributions in Al-Cu-based alloys," *Phys. Rev. B*, vol. 51, pp. 14035 - 14047, 1995.

[7] V. Fournée, E. Belin-Ferré and J. M. Dubois, "Study of Al-Cu Hume-Rothery alloys and their relationship to the electronic properties of quasicrystals," *J. Phys.: Condens. Mat.*, vol. 10, pp. 4231 - 4244, 1998.

[8] Z. Dankhazi, G. T. de Laissardière, E. Belin, D. N. Manh and D. Mayou, "Theoretical and experimental electronic distributions in Al_6Mn," *J. Phys.: Condens. Mat.*, vol. 5, pp. 3339 - 3350, 1993.

[9] Z. M. Stadnik, D. Purdie, M. Garnier, Y. Baer, A. P. Tsai, A. Inoue, K. Edagawa, S. Takeuchi and K. H. J. Buschow, "Electronic structure of quasicrystals studied by ultrahigh-energy-resolution photoemission spectroscopy," *Phys. Rev. B*, vol. 55, pp. 10938 - 10951, 1997.

[10] Z. M. Stadnik, D. Purdie, Y. Baer and T. A. Lograsso, "Absence of fine structure in the photoemission spectrum of the icosahedral Al-Pd-Mn quasicrystal ," *Phys. Rev. B*, vol. 64, pp. 214202.1 - 6, 2001.

[11] P. J. Black, "The Structure of $FeAl_3$," *Acta. Cryst.*, vol. 8, pp. 43 - 48, 1955.

[12] J. Grin, U. Burkhardt and M. Ellner, "Refinement of the Fe_4Al_{13} structure and its relationship to the quasihomological homeotypical structures," *Z. Kristallogr.*, vol. 209, pp. 479 - 487, 1994.

[13] P. Volkov and S. J. Poon, "Anomalous electrical resistivities of decagonal approximants," *Phys. Rev. B*, vol. 52, pp. 12685 - 12689, 1995.

[14] T. Fujiwara and T. Yokokawa, "Universal pseudogap at the fermi energy in quasicrystals," *Phys. Rev. Lett*, vol. 66, pp. 333 - 336, 1991.

[15] G. Trambly de Laissardière, D. Nguyen-Manh and D. Mayou, "Electronic structure of complex spd Hume-Rothery phases in transitionCmetal aluminides," in *The Science of Complex Alloy Phases*. P. Turchi and T. Massalski, eds., Warrendale, PA: TMS, 2005, pp. 345 - 372.

[16] F. Müller, M. Rosenberg, W. Liu and U. Köster, "Mössbauer measurements and susceptibility measurements on crystalline and icosahedral AlCuFe alloys," *Mater. Sci. and Eng.*, vol. A134, pp. 900 - 903, 1991.

[17] R. A. Brand, J. Pelloth, F. Hippert and Y. Calvayrac, "Correlations in the electronic properties of AlCuFe quasicrystals and high-order approximants: ^{57}Fe Mössbauer, and ^{27}Al and ^{65}Cu nuclear magnetic resonance studies," *J. Phys.: Condens. Mat.*, vol. 11, pp. 7523 - 7543, 1999.

[18] Thermodata nuclear database, http://www.crct.polymtl.ca/FACT/documentation/TDNucl/Fe.jpg, 2007

[19] U. Burkhardt, Y. U. Grin and M. Ellner, "Structure refinement of the iron-aluminium phase with the approximate composition," *Acta. Cryst.*, vol. B50, pp. 313 - 316, 1994.

[20] R. N. Corby and P. J. Black, "Structure of $FeAl_2$ by anomalous dispersion methods," *Acta. Cryst.*, vol. 29, pp. 2669 - 2677, 1973.

[21] C. S. Lue, Y. Öner, D. G. Naugle and J. H. Ross, Jr., "Spin glass behavior in $FeAl_2$," *Phys. Rev. B*, vol. 63, pp. 184405.1 - 4, 2001.

[22] C. S. Lue and Y.-K. Kuo, "Thermal and electrical transport properties of ordered $FeAl_2$," *J. Phys.: Condens. Matter*, vol. 15, pp. 877 - 882, 2003.

[23] P. J. Brown, "The structure of α(V-Al)," *Acta Cryst.* , vol. 10, pp. 133 - 135, 1957.

[24] M. Jahnátek, M. Krajčí and J Hafner, "Electronic structure and interatomic bonding in $Al_{10}V$," *J. Phys.: Condens. Matter*, vol. 15, pp. 5675 - 5688, 2003.

[25] A. D. Caplin, G. Gruner and J. B. Dunlop, "$Al_{10}V$ - Einstein Solid," *Phys. Rev. Lett.*, vol. 15, pp. 1138 - 1140, 1973.

[26] S. Jia, S. L. Budko, G. D. Samolyuk and P. C. Canfield, "Nearly ferromagnetic Fermi-liquid behavior in YFe_2Zn_{20} and high-temperature ferromagnetism of $GdFe_2Zn_{20}$," *Nature Physics*, vol. 3, pp. 334 - 338, 2007.

[27] V. M. T. Thiede, W. Jeitschko, S. Niemann and T. Ebel, "$EuTa_2Al_{20}$, $Ca_6W_4Al_{43}$ and other compounds with $CeCr_2Al_{20}$ and $Ho_6Mo_4Al_{43}$ type structures and some magnetic properties of these compounds," *J. Alloys Compd.*, vol. 267, pp. 23 - 31, 1998.

[28] D. Guenzburger and D. E. Ellis, "Fe impurity in Al — magnetic or nonmagnetic," *Phys. Rev. Lett.*, vol. 67, pp. 3832 - 3835, 1991.

[29] M. Jaime, R. Movshovich, G. R. Stewart, W. P. Beyermann and M. G. Berisso, M. F. Hundley, P. C. Canfield and J. L. Sarrao, "Closing the spin gap in the Kondo insulator $Ce_3Bi_4Pt_3$ at high magnetic fields," *Nature*, vol. 405, pp. 160 - 163, 2000.

[30] K. Sugiyama, F. Iga, M. Kasaya, T. Kasuya and M. Date, "Field-induced metallic state in YbB_{12} under high magnetic-Field," *J. Phys. Soc. Jpn.*, vol. 57, pp. 3946 - 3953, 1988.

[31] J. C. Cooley, C. H. Mielke, V. L. Hults, J. D. Goettee, M. M. Honold, R. M. Modler, A. Lacerda, D. G. Rickel and J. L. Smith, "High field gap closure in the Kondo insulator SmB_6," *J. Supercond.*, vol. 12, pp. 171 - 173, 1999.

[32] S. Gabáni, E. Bauer, S. Berger, K. Flachbart, Y. Paderno, C. Paul, V. Pavlík and N. Shitsevalova, "Pressure-induced Fermi-liquid behavior in the Kondo insulator

SmB_6: Possible transition through a quantum critical point," *Phys. Rev. B*, vol. 67, pp. 172406.1 - 4, 2003.

[33] S. Yeo, S. Nakatsuji, A. D. Bianchi, P. Schlottmann, Z. Fisk, L. Balicas, P. A. Stampe and R. J. Kennedy, "First-order transition from a Kondo insulator to a ferromagnetic metal in single crystalline $FeSi_{1-x}Ge_x$," *Phys. Rev. Lett.*, vol. 91, pp. 046401.1 - 4, 2003.

[34] T. Ohashi, A. Koga, S. Suga and N. Kawakami, "Field-induced phase transition in a Kondo insulator," *Phys. Rev. B*, vol. 70, pp. 245104.1 - 6, 2004.

[35] C. P. Slichter, *Principles of Magnetic Resonance,* New York: Springer-Verlag, 1990.

[36] A. Abragam, *Principles of Nuclear Magnetism,* London: Oxford University Press, 1982.

[37] A. Narath, "Nuclear spin-lattice relaxation in hexagonal transition metals: titanium," *Phys. Rev.*, vol. 162, pp. 320 - 332, 1967.

[38] B. H. Toby, "EXPGUI, a graphical user interface for GSAS," *J. Appl. Cryst.*, vol. 34, pp. 210 - 213, 2001.

[39] A. C. Larson and R. B. von Dreele, "General structure analysis system (GSAS)," LAUR 86-748, Los Alamos National Laboratory, 2000.

[40] G. C. Carter, L. H. Bennett and D. J. Kahan, *Metallic Shifts in NMR,* Oxford: Pergamon, 1977.

[41] C. S. Lue and J. H. Ross, Jr., "Correlated electron behavior in Al_3V: NMR evidence," *Phys. Rev. B*, vol. 60, pp. 8533 - 8539, 1999.

[42] Y. D. Zhang, J. I. Budnick, F. H. Sanchez and R. Hasegawa, "NMR study of rapidly quenched $Fe_{95}M_5$ crystalline alloys," *J. Appl. Phys.*, vol. 67, pp. 5870 - 5872, 1990.

[43] J. J. Spokas, C. H. Sowers, Van Ostenburg, D. O. and H. G. Hoeve, "Nuclear magnetic resonance in cubic equiatomic group-VIII aluminides," *Phys. Rev. B*, vol. 1, pp. 2523 - 2531, 1970.

[44] D. Rau, J. L. Gavilano, Sh. Mushkolaj, C. Beeli, M. A. Chernikov and H. R. Ott, "Anomalous magnetism in decagonal $Al_{69.8}Pd_{12.1}Mn_{18.1}$," *Phys. Rev. B*, vol. 68, pp. 134204.1 - 8, 2003.

[45] R. E. Watson and M. Weinert, "Transition-metal aluminide formation: Ti, V, Fe, and Ni aluminides," *Phys. Rev. B*, vol. 58, pp. 5981 - 5988, 1998.

[46] M. Krajčí and J. Hafner, "Covalent bonding and bandgap formation in transition-metal aluminides: di-aluminides of group VIII transition metals," *J. Phys.: Condens. Matter*, vol. 14, pp. 5755 - 5783, 2002.

[47] M. C. Chen and C. P. Slichter, "Zero-field NMR study on a spin glass: Iron-doped 2H-niobium diselenide," *Phys. Rev. B*, vol. 27, pp. 278 - 292, 1983.

[48] J. L. Gavilano, D. Rau, Sh. Mushkolaj, H. R. Ott, J. Dolinsěk and K. Urban, "Anomalous NMR response of quasicrystalline icosahedral $Al_{72.4}Pd_{20.5}Mn_{7.1}$ at low temperatures," *Phys. Rev. B*, vol. 65, pp. 214201.1 - 8, 2002.

[49] Toru Moriya, *Spin Fluctuations in Itinerant Electron Magnetism,* Berlin: Springer-Verlag, 1985.

[50] J. Dolinšek, M. Klanjšek, T. Apih, A. Smontara, J. C. Lasjaunias, J. M. Dubois,

S. J. Poon, "Searching for sharp features in the pseudogap of icosahedral quasicrystals by NMR," *Phys. Rev. B*, vol. 62, pp. 8862 - 8870, 2000.

[51] A. Narath, "Nuclear magnetic resonance in magnetic and metallic solids," in *Hyperfine Interactions*. A. J. Freeman and R. B. Frankel, eds., New York: Academic Press, 1967, pp. 287 - 363.

[52] N. W. Ashcroft and N. D. Mermin, *Solid State Physics,* New York: Saunders College, 1976.

[53] J. Hafner and M. Krajčí, "Formation of magnetic moments in crystalline, quasicrystalline, and liquid Al-Mn alloys," *Phys. Rev. B*, vol. 57, pp. 2849 - 2860, 1998.

[54] P. Shukla and M. Wortis, "Spin-glass behavior in iron-aluminum alloys: A microscopic model," *Phys. Rev. B*, vol. 21, pp. 159 - 164, 1980.

[55] O. Kanert and M. Mehring, "Static quadrupole effects in disordered cubic solids," in *NMR: Basic Principles and Progress*. E. Fluck and R. Kosfeld, eds., New York: Springer-Verlag, 1971, pp. 1 - 81.

[56] X.-P. Tang, E. A. Hill, S. K. Wonnell, S. J. Poon and Y. Wu, "Sharp feature in the pseudogap of quasicrystals detected by NMR," *Phys. Rev. Lett.*, vol. 79, pp. 1070 - 1073, 1997.

[57] J. Dolinšek and M. Klanjšek and T.Apih, "Paramagnetic NMR relaxation in icosahedral quasicrystals," *Ferroelectrics*, vol. 250, pp. 195 - 200, 2001.

[58] J. Winter, *Magnetic Resonance in Metals,* Oxford: Claredon, 1971.

[59] Ji Chi, Yang Li, F. G. Vagizov, V. Goruganti and Ross, Jr., Joseph H., "NMR and Mössbauer study of spin-glass behavior in $FeAl_2$," *Phys. Rev. B*, vol. 71, pp. 24431.1 - 5, 2005.

[60] J. Dolinšek, M. Klanjšek, T.Apih, J. L. Gavilano, K. Gianno, H. R. Ott, J. M. Dubios and K. Urban, "Mn magnetism in icosahedral quasicrystalline $Al_{72.4}Pd_{20.5}Mn_{7.1}$," *Phys. Rev. B*, vol. 64, pp.024203.1 - 8, 2001.

[61] P. Jeglič and J. Dolinšek, "NMR features of a decagonal $Al_{72.6}Ni_{10.5}Co_{16.9}$ quasicrystal," *Phys. Rev. B*, vol. 71, pp. 014204.1 - 11, 2005.

[62] T. Schaub, J. Delahaye, C. Gignoux, C. Berger, G. Fourcaudot, F. Giroud, T. Grenet and A. G. M. Jansen, "Pseudogap in quasicrystals probed by tunneling spectroscopy," *J Non Cryst Solids*, vol. 250, pp. 874 - 877, 1999.

[63] J. Delahaye, T. Schaub, C. Berger and Y. Calvayrac, "Scanning tunneling spectroscopy on oxidized surfaces of highly resistive quasicrystalline alloys," *Phys. Rev. B*, vol. 67, p. 214201.1 - 17, 2003.

[64] G. Li, H. He, Y. Wang, L. Lu, S. Li, X. Jing and D. Zhang, "Tunneling spectroscopy in AlNiCo decagonal quasicrystals," *Phys. Rev. Lett.*, vol. 82, pp. 1229 - 1232, 1999.

[65] C. Berger, D. Mayou, T. Grenet, Z. Ovadyahu, "Comment on "Tunneling spectroscopy in AlNiCo decagonal quasicrystal"," *Phys. Rev. Lett.*, vol. 83, p. 3968 - 3968, 1999.

[66] E. Belin-Ferré, "Electronic Structure in Quasicrystalline Compounds and Related Crystals," *J. Phys.: Condens. Matter*, vol. 14, pp. R789 - R817, 2002.

[67] A. Cezairliyan, "Specific heats of solids," in *Cindas Data Series on Material Properties*. Y. S. Touloukian and C. Y . Ho, eds., New York: Hemisphere Publishing Corporation, 1988, vol.I-2.

[68] R. L. Falge, Jr. and N. M. Wolcott, "Cluster specific heats in copper-rich Cu-Ni Alloys: the effects of iron," *J. Low Temp. Phys*, vol. 5, pp. 617 - 650, 1971.

[69] H. Meštrić, R.-A. Eichel, K.-P. Dlinse, A. Ozarowski, J. V. Tol and L. C. Brunel, "High-frequency electron paramagnetic resonance investigation of the Fe^{3+} impurity center in polycrystalline $PbTiO_3$ in its ferroelectric phase," *J. Appl. Phys.*, vol. 96, pp. 7440 - 7444, 2004.

[70] R. A. Dunlap, D. J. Lloyd, I. A. Christie, G. Stroink and Z. M. Stadnik, "Physical-properties of rapidly quenched Al-Fe alloys," *J. Phys. F: Met. Phys.*, vol. 18, pp.1329 - 1341, 1988.

[71] J. Chi, Y. Li, W. Gou, V. Goruganti, K. D. D. Rathnayaka and J. H. Ross, Jr., "Pseudogap and dilute magnetism in decagonal approximant Fe_4Al_{13}," *submitted to Phys. Rev. B.*, 2007

[72] M. B. Tang, H. Y. Bai and W. H. Wang, "Tunneling states and localized mode in binary bulk metallic glass," *Phys. Rev. B.*, vol. 72, pp. 012202.1 - 4, 2005.

[73] W. L. McMillan, "Scaling theory of the metal-insulator transition in amorphous materials," *Phys. Rev. B*, vol. 24, pp. 2739 - 2743, 1981.

[74] J. Hafner, "Electronic structure of quasicrystals," *Current Opinion in Solid State & Materials Science*, vol. 4, pp. 289 - 294, 1999.

[75] F. S. Pierce, S. J. Poon and Q. Guo, "Electron localization in metallic quasicrystals," *Science*, vol. 261, pp. 737 - 739, 1993.

[76] K. Ghoshray, B. Bandyopadhyay and A. Ghoshray, "NMR study of the electronic state in the dense Kondo compound $CeNiAl_4$," *Phys. Rev. B*, vol. 65, pp. 174412.1 - 6, 2005.

[77] E. Kim and D. L. Cox, "Knight-shift anomalies in heavy-electron materials," *Phys. Rev. B*, vol. 58, pp. 3313 - 3340, 1998.

[78] T. Vojta, "Quantum phase transitions in electronic systems," *Ann. Phys.*, vol. 9, pp. 403 - 440, 2000.

[79] G. R. Stewart, "Non-Fermi-liquid behavior in d- and f-electron metals," *Rev. Mod. Phys.*, vol. 73, pp. 797 - 855, 2001.

[80] S. Nakamura, M. Endo, H. Aoki, N. Kimura and T. Nojima, "Field-induced transition from non-Fermi-liquid state to heavy Fermion state in $Ce_{0.5}La_{0.5}B_6$," *Phys. Rev. B*, vol. 68, pp. 100402.1 - 4, 2003.

[81] Y. Aoki, T. Namiki, T. D. Matsuda, K. Abe, H. Sugawara and H. Sato, "Anomalous heavy-fermion and ordered states in the filled skutterudite $PrFe_4P_{12}$," *Phys. Rev. B*, vol. 65, pp. 064446.1 - 7, 2002.

VITA

Ji Chi, 20 Brickyard Dr. Apt. C22, Bloomington, IL.

Ji Chi was born January 9, 1978 in Anhui, China. He received his bachelor's degree in physics from the University of Science and Technology of China. He got his Master's degree in Condensed matter experimental Physics from Texas A&M University in 2003. His email address is club_hutong@hotmail.com.